ABSTRACT

Title of Document: EFFECTS OF CERIA ADDITION ON NICKEL/YSZ ANODES IN SOLID OXIDE FUEL CELLS OPERATING ON HYDROGEN AND SYNGAS FUEL FEEDS

Paul Francis Jawlik, Master of Science, 2008

Directed By: Associate Professor, Dr. Gregory Jackson, Mechanical Engineering

Anode-supported solid oxide fuel cells (SOFCs) utilizing Ni/Ceria-YSZ composite anode architectures were designed, built, and tested on hydrogen and syngas fuel feeds to evaluate the effect of adding ceria (CeO_2) to Ni/YSZ anodes. All anodes were approximately 1.0 mm thick and composed of two layers: a thick, high-porosity support layer and a thin low-porosity (20-30%) functional layer, 20 to 25 μm thick. Three different anode architectures containing CeO_2 were tested and compared with each other and with a baseline Ni/YSZ anode. CeO_2 containing cells made using a co-firing method of fabrication produced maximum power densities of 0.60 and 0.33 W/cm^2 for operation on syngas while the Ni/YSZ cell produced 0.26 W/cm^2. Comparison of the high and low frequency arcs observed in the impedance spectra (attributed to the anode and cathode respectively) indicate that a reduced anode polarization resistance for cells containing CeO_2 is due principally to improved microstructure in the anode support layer. However, for syngas operation there is

also evidence that improved electrocatalytic activity with the H_2 and CO mixture occurs with CeO_2 present in the anode support and/or functional layers.

EFFECTS OF CERIA ADDITION ON NICKEL/YSZ ANODES IN SOLID OXIDE FUEL CELLS OPERATING ON HYDROGEN AND SYNGAS FUEL FEEDS

By

Paul Francis Jawlik

Thesis submitted to the Faculty of the Graduate School of the
University of Maryland, College Park, in partial fulfillment
of the requirements for the degree of
Master of Science
2008

Advisory Committee:
Professor Gregory Jackson, Chair
Professor Hugh Bruck
Professor Bryan Eichhorn

Acknowledgements

I would first like to thank Steven DeCaluwe and Siddharth Patel. Steven's patient answering of my many questions regarding fundamental SOFC processes provided me with a more intricate understanding of SOFCs than I could have ever gained on my own. Siddharth's help in setting up and running experiments, brainstorming over rig designs, and running fits was critical to the completion of this work.

I would also like to thank the many other graduate students that fall under Dr. Jackson's umbrella of advising. Jenny Hu, Joshua Pearlman, and Atul Bhargav deserve particular thanks for the miscellaneous help they provided over the last two years. Several graduate student colleagues in the Chemistry Department are also deserving of my gratitude: Bryan Eigenbrodt, Anthony Dylla, and Selim Alayogluwere helpful in answering many of my questions requiring the knowledge of a chemist.

Thanks also to Dr. Mary Sukeshini for patiently teaching me the basics of SOFCs, Ian Young for his help in designing a new rig, Anita Maghdouri for help in fabricating cells, and Eric Shields for his pep talks during bleak times. Larry Lai and Dr. Wen-An Chiou should also be acknowledged for helping me operate the SU-70 Hitachi SEM. Dr.'s Bryan Eichhorn and Robert Walker provided insightful and helpful recommendations during group meetings and informal encounters in the hallway. Thank you.

I would also like to acknowledge the Petroleum Institute for generously funding this research and Dr. Bryan Eichhorn and Dr. Hugh Bruck for graciously sitting on my defense committee.

My family and friends who have not been mentioned are also deserving of my thanks for their continued support and encouraging words.

Lastly, I would like to offer immense thanks to Dr. Jackson for his role as my advisor. Nearly every step of this research has been more difficult than I initially imagined. Dr. Jackson's extensive SOFC knowledge and general laboratory know-how, however, led to consistent (albeit slow) progress despite the significant challenges that were faced. His patience and constructive criticism have also been invaluable to the completion of this work and have made me into a better scientist and engineer.

Table of Contents

List of Tables

List of Figures

Nomenclature

Symbol	Description
A	Pre-exponential
a	Subscript used to denote the anode
c	Subscript used to denote the cathode
D	Reactant diffusion coefficient at 300 K
$D_{eff,\,k}$	Effective ion diffusion coefficient through the electrolyte
E_a	Activation energy
F	Faraday's constant
G	Gibbs free energy
H	Enthalpy
i	Current density
i_{leak}	Leakage current
i_{limit}	Limiting current density
i^0	Exchange current density
n_{el}	Number of electrons exchanged in a specified reaction
n_T	Temperature correction for D
n_{O2}	Molar flux of O_2
P_k	Partial pressure of species k
R	Universal gas constant
R_{bulk}	Bulk resistance
R_{pol}	Polarization resistance
R_{tot}	Total resistance
S	Entropy
T	Temperature
V_a	Actual voltage
V_{rev}	Nernst Voltage
$W_{e,rev}$	Maximum extractable work from an electrochemical reaction
Z	Impedance
Z_0	Magnitude of the Impedance
Z'	Real component of the impedance
Z''	Imaginary component of the impedance
β_f	Forward reaction charge transfer coefficient
β_r	Reverse reaction charge transfer coefficient
$\eta_{act,\,-}$	Activation overpotential due to a specified entity - (i.e. anode, Cell 1, etc.)
η_a	Anode overpotential
η_c	Cathode overpotential
$\eta_{conc,\,-}$	Concentration overpotential due to a specified entity - (i.e. anode, Cell 1, etc.)
η_{ohm}	Ohmic overpotential
η_{tot}	Total overpotential

Φ	Phase difference between voltage and current signals
σ	Conductivity

ACRONYMS

ASR	Area Specific Resistance
CTE	Coefficient of Thermal Expansion
DAQ	Data Acquisition System
EDS	Energy Dispersive Spectroscopy
EIS	Electrochemical Impedance Spectroscopy
LSV	Linear Sweep Voltammetry
MEA	Membrane Electrode Assembly
MFC	Mass Flow Controlloer
OCV	Open Circuit Voltage
OP	Overpotential
PEMFC	Proton Exchange Membrane Fuel Cell
SEM	Scanning Electron Microscope
SOFC	Solid Oxide Fuel Cell
TC	Thermocouple
TPB	Three Phase Boundary
V-I	Voltage-Current
WGS	Water Gas Shift Reaction

Chapter 1: Introduction

1.1 Solid Oxide Fuel Cells

Solid oxide fuel cells (SOFCs) are a promising clean, efficient energy technology. As they directly convert chemical energy to electrical energy, they can be more efficient than combustion based technologies. Additionally, as the fuel and oxidant never mix during operation and the operating temperatures generally do not exceed 1000 °C, SOFCs have the potential to operate with little to no NO_x. For operation with hydrogen as the fuel, SOFCs are particularly clean, with emissions consisting of only water. What truly make SOFCs an exciting technology, however, is their ability to run on fuels other than hydrogen. Fuels such as carbon monoxide, syngas (defined here as flows containing CO, H_2, CO_2, and H_2O), methane, and other hydrocarbons that are all currently poisonous to lower-temperature proton exchange membrane fuel cells (PEMFCs), can all be theoretically used in a properly designed SOFC. In this regard SOFCs have the promise of being readily integrated into current, hydrocarbon-oriented energy infrastructures. Operation on hydrocarbon fuels does generate carbon dioxide, but as it is straightforward to isolate it from exhaust streams, SOFCs are an ideal candidate for integration with carbon sequestration strategies.

While SOFCs show significant promise for future power generation, outstanding development issues must be addressed before they can see wide-spread

penetration in both small- and large-scale power applications. The need to use ceramic electrolyte materials at operating temperatures of 600 to 1000 °C results in lengthy start up times (>10 minutes) and the cells can be prone to cracking during rapid thermal cycling. Additionally, when operating on carbonaceous fuels, SOFCs can catalyze the formation of solid carbon [1]. This carbon covers catalytically active portions of the cell and leads to a reduction in performance.

The appeal of a fuel flexible power system with low levels of pollution is strong enough, however, that SOFCs are being considered for many applications despite their developmental challenges. The potential applications range in size from large-scale power generation (megawatts), to small-scale stationary plants (kilowatts), to auxiliary power units in automobiles and aircraft. Recently, private companies have begun to extend the range of applications even further. Fifty watt scale systems are being designed to meet the portable energy demands of the 21st century soldier and SOFCs based on microfabrication techniques are being designed to provide power for portable electronic devices.

The application that motivates the current study is the use of SOFCs to convert oil well off-gases to electrical power. In many petroleum processing facilities, undesirable gases encountered during day-to-day operations are flared in an effort to dispose of combustible materials in a safe and environmentally friendly way (the greenhouse gas heating value of the product gases being less than that of the reactant gases). Instead of flaring off-gases and wasting a potential energy source, these gases may be passed through an SOFC to generate electricity. As an added benefit, the CO_2 and H_2O in the SOFC exhaust stream can be captured and injected

into onsite wells for the purposes of enhanced oil recovery and/or carbon sequestration.

1.2 SOFC Fundamentals

1.2.1 Basic Operation

The heart of an SOFC is the membrane-electrode assembly (MEA), as shown in Figure 1.1. An SOFC MEA is composed of three main components: an anode, a cathode, and an electrolyte. Fuel enters the gas flow channels on the anode side. The porous anode contains an electrocatalyst that facilitates the oxidation of the fuel by O^{2-} ions supplied from the O^{2-} ion-conducting electrolyte as described by Reaction 1.1.

$$H_2(g) + O^{2-}(el) \longrightarrow H_2O(g) + 2e^-(a) \qquad \text{(R1.1)}$$

This generates free electrons which exit the cell, travel through an external circuit, and perform work. On the cathode side, a flow containing molecular oxygen enters the cathode-side flow channels. The cathode contains an O_2-reducing electrocatalyst that facilitates the splitting of the O_2 into two O^{2-} ions as described by Reaction 1.2.

$$\tfrac{1}{2} O_2(g) + 2e^-(c) \longrightarrow O^{2-}(el) \qquad \text{(R1.2)}$$

The electrons in the external circuit are routed to the cathode and supply the electrons for this reaction. The voltage difference generated between the anode and the cathode by the electrochemical reactions drives the O^{2-} ions through the electrolyte to the anode. The global reaction is given by Reaction 1.3.

$$H_2(g) + \tfrac{1}{2}O_2(g) \longrightarrow H_2O(g) \qquad \text{(R1.3)}$$

In all reactions parenthesis indicate phase with (a) designating the anode, (el) the electrolyte, (c) the cathode, and (g) gas.

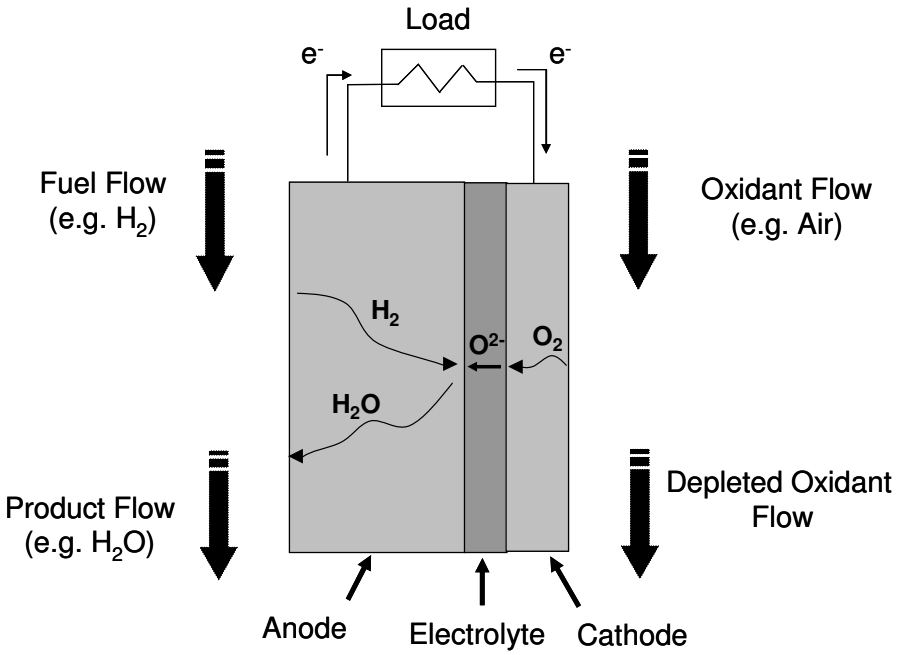

Figure 1.1 The basic operation of a solid oxide fuel cell membrane electrode assembly (MEA) utilizing H_2 as a fuel and a parallel flow geometry

For fundamental characterization of MEAs, button cell geometries are used with impinging flow fields on the surface of each porous electrode. This flow arrangement, which is used in the current study, provides near uniform mass transfer

across the surface of each electrode. Another common flow geometry is the parallel flow geometry in which the inlet side of the cell is exposed to a fuel and oxidant rich gas mixture while the outlet side of the cell is exposed to a fuel and oxidant lean mixture. Impinging flow geometries are preferred when there is a desire to understand cell behavior on specific gases or gas mixtures, and typically flow rates are set such that fuel and oxidant utilizations are low (< 10%). Parallel flow geometries are more practical for real applications as the fuel and oxidant utilizations are normally higher than that for the impinging flow geometry.

The oxidation of fuel and the reduction of oxygen are generally thought to occur along interfaces between the electrocatalyst, electrolyte, and gas phases. This interface is referred to as the three phase boundary (TPB). The length of the TPB is enhanced by mixing micron or submicron electrolyte-phase particles and electrocatalyst particles in the electrochemically active regions of the electrodes near the dense electrolyte, as exemplified by the schematic in Figure 1.2. The electrolyte phase supplies (anode side) or removes (cathode side) O^{2-} ions to or from areas of electrochemical oxidation or reduction respectively. As the electrolyte phase is conventionally dispersed in micron-sized particles throughout both electrodes, TPB regions are found throughout both electrodes. The O^{2-} ions, however, tend to travel only short distances (on the order of tens of microns) beyond the electrolyte [2]. This means that electrochemical reactions only take place along the TPB in regions at or near the dense electrolyte membrane in what is often referred to as the functional layer. Outside the functional layer, all three phases may be simultaneously present,

but the O^{2-} ion will have been largely consumed in the functional layer and there will be minimal electrochemical activity.

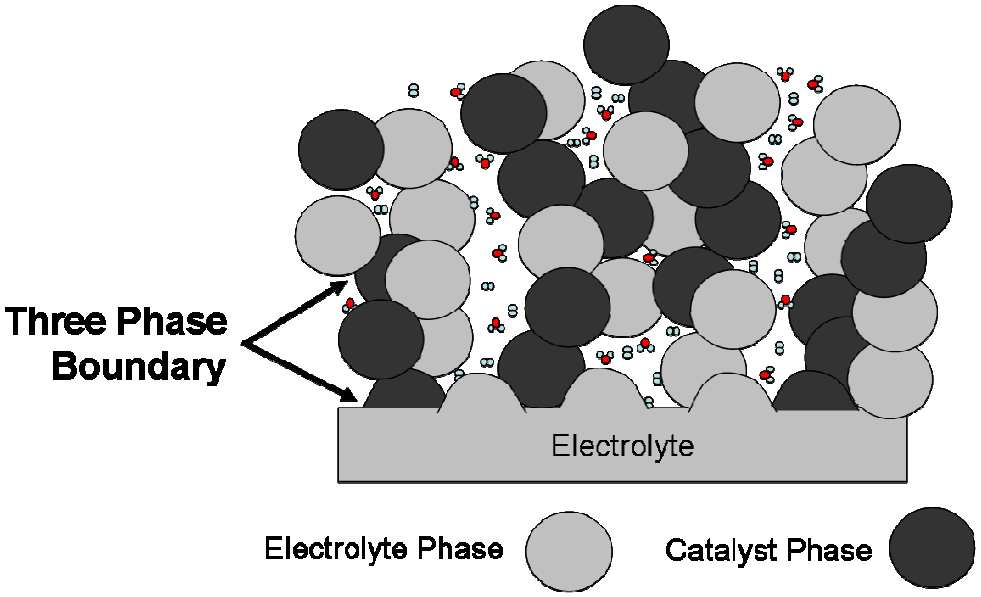

Figure 1.2 The three phase boundary

The anode, cathode, or electrolyte must form the structural backbone of the cell in order to minimize the risk of cracks, warps, and other cell deformations. The thickness of the support structure is usually between 0.5 and 1.0 mm. For most practical SOFC MEAs, the porous anode is used to support the cell, and as such the fuel and oxidation products must diffuse a significant distance through the anode media. The other MEA components are relatively thin by comparison, normally less than 100μm in total thickness. In applications where high power densities are desired (> 0.3 W/cm^2 of active cell area), the thick anode is accompanied by a very thin electrolyte membrane (< 20μm) and a porous cathode that minimizes resistance to gas phase transport. In these applications the dense electrolyte membrane is not selected

as the support structure because of the relatively high resistance to O^{2-} transport at SOFC operating temperatures.

1.2.2 Anode Design

Most high power density applications exploit anode-supported geometries. This is preferred over cathode-supported geometries because typical anode gases such as H_2 have faster diffusion rates through the porous media than typical cathode gases such as air. This ease of diffusion is important because the oxidation reactions occur deep inside the anode near the electrolyte membrane.

The oxidation reactions inside the anode are facilitated by electrocatalysts. Some electrocatalysts like Ni have high electronic conductivities ($\sigma_{elec,Ni}$ ~ 1e5 S/cm @ 25 °C) and can conduct electrons to external circuits without significant ohmic losses, while other active materials like CeO_2 do not provide such high conductivity values ($\sigma_{elec,CeO2}$ ~ 0.1 S/cm @ 800 °C [3]) and are therefore often mixed with highly conductive current-collecting materials such as Cu [1, 4-6]. For most applications, conductivity of the porous anode should be above 100 S/cm to avoid significant ohmic loses due to electron transport [3].

In addition to the catalyst, it is also important to incorporate O^{2-} conducting electrolyte material into the anode. This material provides structural support and ensures adequate binding and CTE matching between the anode and the electrolyte membrane. The electrolyte phase in the anode provides pathways for O^{2-} ion migration, effectively extending the electrochemically active zone beyond the two-dimensional anode/electrolyte interface.

In an effort to maximize TPB length in the electrochemically active region, high performance anodes often incorporate a thin, low porosity (20-30%) functional layer [2]. In an effort to ensure extensive catalyst and electrolyte surface exposure, particle and pore sizes are smaller than those in the support layer (~0.5-1μm in the functional layer compared to ~1–10μm in the support layer) [7]. Although the lower porosity makes gas diffusion more difficult, pressure drops are minimized by making the layer only as thick as the distance oxygen ions migrate into the anode. This translates into a typical functional layer thickness between 20 and 30μm [2].

1.2.3 Cathode and Electrolyte Design

The cathode should be porous and contain catalyst particles to split O_2 and ionically-conducting material to transport the resulting O^{2-} ions to the electrolyte. If the anode is providing support for the cell, the cathode should be thin (< 100 μm) so as to minimize O_2 concentration losses and electrical resistance of the cathode. Some SOFC architectures utilize bi-layer cathodes consisting of a low porosity functional layer and a secondary current collecting layer [8, 9]. Other architectures employ a single low porosity functional layer [10-12]. In both configurations the cathode functional layer serves the same purpose as the anode functional layer. The secondary (current-collecting) layer provides cross-plane conductivity pathways for the incoming electrons, allowing for a uniform electron distribution within the functional layer. This layer should be more porous than the functional layer and only contain the conductive phase species.

The electrolyte membrane conducts O^{2-} ions from the cathode to the anode without allowing electron transport. The membrane must provide a gas-tight seal to minimize leakage between electrodes. The most common electrolyte material used in commercial SOFC applications is yttria-stabilized zirconia, YSZ, which has strong O^{2-} ion conductivity above 700 ºC and relatively no electron conductivity at these high temperatures.

As O^{2-} conduction improves with temperature, it is desirable from a performance perspective to operate at temperatures approaching 1000 ºC. These temperatures, however, require the use of expensive materials for some of the support components (pastes, wires, etc) and make sealing around the edges of the MEAs quite problematic. Temperatures near 800 ºC offer the benefits of improved ion conductivity while allowing for the use of cheaper materials for current collection and sealing (i.e. silver instead of gold or platinum). For these reasons 800 – 850 ºC is a common operating temperature for SOFCs with YSZ electrolytes. Significant research is also being performed on electrolyte materials that can operate at even lower temperatures (~ 600 ºC) without incurring significant ohmic losses [12-14]. These alternative materials will allow for cheaper sealing and current collecting materials than with YSZ electrolytes.

To prevent mixing of the anode and cathode gases, and the subsequent drop in voltage, the electrolyte membrane needs to be dense, and relatively free of pinholes and cracks. These requirements are made more difficult by the fact that electrolytes are often the thinnest component of an anode-supported cell and are therefore more prone to material failure. Thicknesses of electrolytes range from 60 μm at the high

end to 8 μm at the low end [8, 11]. Although the electrolyte should be made as thin as possible, its contribution to the ohmic resistance becomes small enough below thicknesses of 8 μm (< 30% at 700 ºC) that further reductions without lower temperatures, result in minimal improvements to cell performance [8].

1.2.4 Performance

For temperatures and pressures typical of an SOFC environment, the maximum extractable work (W_e) is given by the change in Gibbs free energy (ΔG). The change in Gibbs free energy is equal to the total available thermal energy (ΔH) minus the energy caused by changes in entropy ($T\Delta S$). In electrical processes the actual work $W_{e,rev}$ is determined by knowing the amount and energy of the electrons released by an electrochemical reaction. $W_{e,rev}$ is equal to the product of the number of electrons exchanged per reaction (n_{el}), Faraday's constant (F = 96,485 C/mole electrons), and the ideal electric potential of the electrons (V_{rev}). Setting these two expressions for work equal to one another yields Equation 1.1 where T is temperature and P is pressure.

$$W_{e,rev} = \Delta G(T,P) = \Delta H(T,P) - T\Delta S(T,P) = n_{el} F V_{rev} \qquad \text{Eq. 1.1}$$

Plugging in expressions for ΔS, assuming an ideal gas, and performing some algebraic manipulation yields:

$$\Delta G(T,P) = \Delta G(T) + RT \ln\left(\prod_i (P_k^{\nu_k})\right) \qquad \text{Eq. 1.2}$$

Here R is the universal gas constant, p_k is the partial pressure of species k (the partial pressure is used because fuel cells normally operate at pressures low enough that the fugacity can be closely approximated by the partial pressure), and v is the stoichiometric coefficient of species k (positive for reactants, negative for products). Substituting this expression into Equation 1.1 and solving for V_{rev} gives:

$$V_{rev} = \frac{\Delta G(T)}{n_{el}F} + \frac{RT}{n_{el}F}\ln\left(\prod_k (p_k{}^{v_k})\right) \qquad \text{Eq. 1.3}$$

Equation 1.3 is known as the Nernst equation and V_{rev} is known as the Nernst potential. The Nernst potential is the maximum electrical voltage that can be generated in an electrochemical reaction. Since $\Delta G(T)$ can be easily calculated from thermodynamic tables, and the partial pressures of the reactant and product gases are generally known, it is a straightforward exercise to calculate the Nernst potential for a given reaction. For the H_2 oxidation reaction the potential is typically around 1.1V at 800 ºC.

The Nernst potential assumes reversibility of reactions. This assumption, however, is only valid when current is not being drawn from the cell, i.e. at open circuit conditions. The Nernst potential is therefore often referred to as the open circuit voltage (OCV). At conditions other than the OCV where the net flow of charge is non-zero, irreversabilities occur. These irreversabilities lead to voltage losses, or overpotentials, which reduce the amount of energy available for electrical work. There are three types of overpotentials: ohmic overpotentials, concentration overpotentials, and activation overpotentials.

The ohmic overpotential η_{ohm} measures how much a cell resists the flow of electron or O^{2-} current. In SOFCs, O^{2-} current through the electrolyte contributes more to η_{ohm} than electron or O^{2-} current through either the anode or cathode. Losses can be minimized, however, by making the electrolyte as thin as possible. The anode, the cathode, the leads running to and from the cell, and the interfaces between cell components also contribute to η_{ohm} as they all resist the flow of charge. η_{ohm} can be calculated by Ohm's Law (Equation 1.4) where i is the current per unit electrolyte area and R_{ohm} is the ohmic area specific resistance (ASR).

$$\eta_{ohm} = iR_{ohm} \qquad \text{Eq. 1.4}$$

Pressure losses experienced by gases diffusing through the anode or cathode result in concentration overpotentials, η_{conc} (sometimes called mass transport overpotentials). This is because the reactant and product partial pressures play a significant role in determining the Nernst voltage (see Equation 1.3). If for example, a reactant species experiences a significant partial pressure drop in traveling through the porous anode than the species partial pressure, and therefore the Nernst potential, will be lower than if the gas experienced a small pressure drop. Increasing porosity and lowering tortuosity in porous electrodes reduces partial pressure drops for reactants coming into electrochemically active functional layers and reduces buildup of product partial pressures in the anode functional layer. As η_{conc} reduces the Nernst potential instead of subtracting from it, it technically is not an overpotential at all.

This technicality, however, is often ignored in the interests of simplicity and convenience.

η_{conc} for both cathode and anode are calculated from Equation 8 where i_{limit} is the limiting current density. The limiting current density occurs when the reactant gases are consumed as fast as they are supplied. At conditions approaching this state, the partial pressure of the reactants goes to zero and the voltage enters a region of steep decline. The limiting current density is calculated from Equation 1.6 where D_k is the effective reactant diffusion coefficient at 300 K and n_T is the temperature correction term for D_k.

$$\eta_{conc} = \frac{RT}{n_{el}F}\ln\left(1-\frac{i}{i_{\lim it}}\right) \qquad \text{Eq. 1.5}$$

$$i_{\lim it} = n_{el}FD_kT^{n_T} \qquad \text{Eq. 1.6}$$

Another source of voltage loss is the activation overpotential (η_{act}). This overpotential is tied to reaction rates and activation barriers that inhibit electrochemical reactions. The charge transfer reaction given by Reaction 1.2 for example, is actually a summation of several reaction steps, each with an associated rate and activation barrier. These steps include O_2 adsorption onto a catalyst, dissociation of the O_2 into surface O atoms, and surface diffusion of O to the TPB (among others)[15]. Each one of these steps lowers the voltage. The sum of all these voltage reductions gives the total activation overpotential.

The Butler-Volmer equation is used to model charge transfer rates (current) in terms of activation overpotentials. It is given by Equation 1.7 where i^0 is the exchange current density and β_f and β_r are the forward and reverse-reaction charge transfer coefficients. Note that η_{conc} cannot be isolated as a function of other variables and therefore must be determined semi-empirically using experimental data and curve fitting tools.

$$i = i^0\left[\exp\left(\frac{\beta_f n_{elec} F \eta_{act}}{RT}\right) - \exp\left(\frac{-\beta_r n_{elec} F \eta_{act}}{RT}\right)\right] \qquad \text{Eq. 1.7}$$

In Equation 1.7, the exchange current density i^0 is the net charge transfer rate in the forward or the reverse direction at open circuit conditions. This is useful because knowing the charge transfer rate at zero current is helpful in determining charge transfer rates at non-zero currents. The exchange current density is determined from Equation 1.8 where A is a pre-exponential coefficient and E_a is the exchange current density activation energy barrier.

$$i^0 = A\exp\left(\frac{-E_a}{RT}\right) \qquad \text{Eq. 1.8}$$

The actual cell potential (V_A) is determined by subtracting all overpotentials from the Nernst potential (Equation 1.9).

$$V_A = V_N - \eta_{ohm} - \eta_{act,a} - \eta_{act,c} - \eta_{conc,a} - \eta_{conc,c} \qquad \text{Eq. 1.9}$$

At low current densities η_{act} tends to be most significant (particularly in the cathode) and causes early drops in voltage. At intermediate current densities, η_{conc} and η_{ohm} become non-negligible and begin to contribute more significantly to the total overpotential. At high current densities, the fuels have trouble reaching the electrochemical region as fast as they are being consumed and η_{conc} becomes more significant and can lead to precipitous drops in voltage. Figure 1.3 shows a classic V-I curve with the combined overpotential (cathode, anode, and electrolyte) shown.

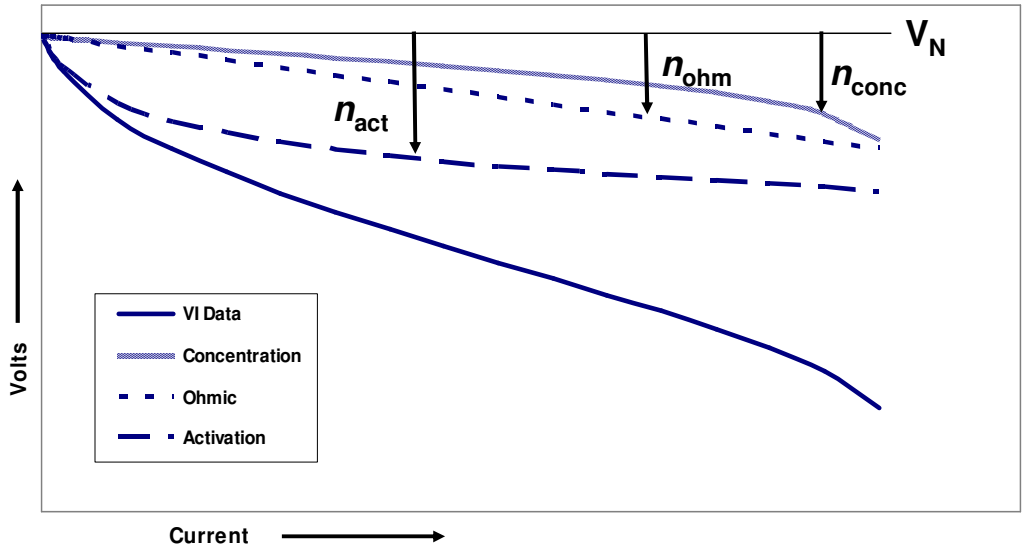

Figure 1.3 V-I curve with component overpotentials

1.2.5 Reforming and Catalysis of Hydrocarbons

As SOFCs can operate on many fuels other than H_2, the reactions for H_2 that are shown in Reactions 1-3 describe a small portion of the possible chemistry SOFCs are capable of supporting. The chemistry, however, becomes more complicated when

other fuels besides H_2 are considered. With the simple addition of carbon monoxide to an existing H_2 flow for example, several additional reactions become possible. CO can be electrochemically oxidized as in Reaction 1.4, reformed via Reaction 1.5, or form solid carbon via the Boudouard reaction, Reaction 1.6. It can also be reduced by H_2 fuel, Reaction 1.7, and under certain conditions the product carbon in Reaction 1.6 and Reaction 1.7 can also be oxidized via Reaction 1.8.

$$CO(g) + O^{2-}(el) \longrightarrow CO_2(g) + 2e^-(a) \quad \text{(R1.4)}$$

$$CO(g) + H_2O(g) \longrightarrow CO_2(g) + H_2(g) \quad \text{(R1.5)}$$

$$2CO(g) \longrightarrow C(s) + CO_2(g) \quad \text{(R1.6)}$$

$$CO(g) + H_2(g) \longrightarrow C(s) + H_2O(g) \quad \text{(R1.7)}$$

$$C(s) + O^{2-}(el) \longrightarrow CO(g) + 2e^-(a) \quad \text{(R1.8)}$$

Which reactions occur is difficult to predict and based on a number of factors including temperature, concentrations, and current loading. Reaction 1.5, called the water-gas-shift (WGS) reaction, is of particular importance as it offers a pathway for transforming CO into H_2.

For hydrocarbons such as methane and butane the reactions are even more numerous and complex. For this reason it is useful to place possible reactions into one of three categories. The first is pyrolysis. Pyrolysis is an endothermic reaction that transforms hydrocarbons into solid carbon and H_2. The general hydrocarbon reaction is given by Reaction 1.9.

$$C_nH_{2n+2}(g) \longrightarrow nC(s) + (n+1)H_2(g) \qquad \text{(R1.9)}$$

The break down of hydrocarbons into H_2 is desirable, but the carbon by-product is not. This is because the carbon can deposit on the anode surface, thereby covering reforming and oxidation sites, reducing porosity, and negatively affecting cell durability [16]. In this regard pyrolysis is to be avoided whenever possible, especially with large hydrocarbons as they deposit proportionately more carbon.

An alternate path for hydrocarbon fuels is that of reforming. In steam reforming, water and hydrocarbons combine to produce CO and H_2 (Reaction 1.10).

$$C_nH_{2n+2}(g) + nH_2O(g) \longrightarrow nCO(g) + (2n+1)H_2(g) \qquad \text{(R1.10)}$$

It is a highly endothermic process (more so than pyrolysis) that can be utilized to prevent carbon deposition. This is because if the steam concentration is high enough, the thermodynamic equilibrium will lean more heavily towards the formation of CO and H_2 via Reaction 1.10 than towards the formation of carbon via Reaction 1.9 (in an analogous manner adding steam to CO increases H_2 production via Reaction 1.7 while decreasing carbon production via Reaction 1.8). As a general guideline carbon deposition can usually be avoided with steam to carbon ratios of 2.5-3 [16].

In addition to steam, CO_2 can also reform hydrocarbons (Reaction 1.11).

$$C_nH_{2n+2}(g) + nCO_2(g) \longrightarrow 2nCO(g) + (n+1)H_2(g) \qquad \text{(R1.11)}$$

CO_2 reforming is also endothermic, but unlike steam reforming it is not always effective in limiting carbon deposition [16]. As far as supplying the necessary energy to sustain these endothermic processes, all energy originates with the exothermic oxidations occurring in the electrochemical region.

A final path a hydrocarbon can take is that of electrochemical oxidation. In this path the hydrocarbons themselves, rather than the product gases, are directly oxidized by the oxygen ions migrating across the electrolyte. The hydrocarbon can undergo partial oxidation producing electrons, H_2, and CO (Reaction 1.12), complete oxidation producing electrons, water, and CO_2 (Reaction 1.13), or some combination of both [16].

$$C_nH_{2n+2}(g) + nO^{2-}(el) \longrightarrow nCO(g) + (n+1)H_2(g) + 2ne^-(a) \qquad \text{(R1.12)}$$

$$C_nH_{2n+2}(g) + (3n+1)O^{2-}(el) \longrightarrow nCO_2(g) + (n+1)H_2O(g) + 2(3n+1)e^-(a) \qquad \text{(R1.13)}$$

Because direct oxidation does not rely on steam, it avoids the energy costs of heating up an additional gas and leads to greater efficiencies. On the other hand, pyrolysis (Reaction 9) and the subsequent deposition of carbon become significant concerns [16].

Instead of directly exposing SOFC anodes to hydrocarbons and letting the cell reform the fuel internally, hydrocarbons can also be reformed externally and the product gases fed to the cell (external reforming). The advantages of external reforming are that the syngas products (CO and H_2) are more easily electrochemically oxidized in the cell than the parent hydrocarbons. Thus, carbon formation is less of a

concern. Although external reforming allows for more stable operation than internal reforming, it requires additional systems that increase the total system complexity.

1.3 Materials

Proper materials selection is critical to the fabrication of high performance SOFCs. First and foremost, the materials must be able to maintain functionality when operating at temperatures from 600-1000 ºC. At these temperatures melting, grain coarsening, and structural weakening are all significant concerns. CTE matches between cell components is also of great significance as the anode, cathode, and electrolyte must expand and contract in relative unison when thermally cycled between room and operating temperatures. For the electrodes, the anode and cathode materials must maintain electrocatalytic activity in reducing and oxidizing environments respectively. The electrolyte must be resistant to both reducing and oxidizing environments.

1.3.1 Electrolyte Materials

Yttria-stabilized zirconia (YSZ) is the most common electrolyte material. It is stable in reducing and oxidizing environments and has a high ionic conductivity and low electronic conductivity even at low P_{O2} [1]. The addition of yttria to zirconia provides crystal stability and oxide vacancies for O^{2-} ion conductivity, with the addition of 8% by mole yttria leading to the highest conductivity [17]. Scandia-stabilized zirconia (ScSZ) is another doped zirconia compound that is used in SOFC

electrolytes. ScSZ has higher conductivity values than YSZ, especially at intermediate temperatures (600-800 ºC), but its conductivity tends to degrade over long periods of operation [18]. Doped CeO_2 is another common electrolyte material. Samarium-doped ceria (SDC) and gadolinium-doped ceria (GDC) are two doped ceria electrolytes that are attractive for low temperature (~500 ºC) operation. Both, however, tend to experience increased electronic conductivities at low oxygen partial pressures [18]. Given its stability, low electronic conductivity, and acceptable ionic conductivity at 800 ºC, YSZ is the preferred electrolyte material for many studies, including this one.

1.3.2 Cathode Materials

The most commonly used cathode catalyst material is Lanthanum Strontium Manganite, $La_{1-x}Sr_xMnO_{3-\delta}$ (LSM). LSM is stable in oxidizing environments, electronically conductive, and has a high electrocatalytic activity for oxygen reduction [19]. YSZ is often mixed in with LSM to increase ionic conductivity and enhance cathode-electrolyte adhesion. Another cathode material is strontium-doped-$LaCoO_3$ (LSC). LSC is attractive as a cathode material because it has a higher catalytic activity than LSM and because it is a mixed ion-electron conductor and therefore does not need to be mixed with YSZ [9]. The downside is the fabrication protocol required to make these cathodes is more complex than the protocol for the traditional LSM cathodes. Other materials such as Sr-doped $LaGaO_3$ (LSGM), Lanthanum Strontium Cobalt Ferrite (LSCF), and Lanthanum Nickelate (LN) have been explored as potential cathode materials as well [20-22].

1.3.3 Anode Materials

Nickel is the most common anode catalyst material. It is cheap, electrocatalytically active, electronically conductive, and does not undergo phase transformations under typical operating conditions [18]. Pure nickel, however, tends to agglomerate and lose pore structure at elevated temperatures [18]. When mixed with the electrolyte material, however, this particle agglomeration is largely mitigated. As an added benefit the electrolyte material improves adhesion with the electrolyte and generates a closer CTE match with the electrolyte.

Ni based anodes, however, can catalyze the formation of carbon when operating on hydrocarbons. This carbon forms on the surface and the interior of the cell, clogging pores and deactivating electrochemical surface sites. Although it can be avoided or minimized by altering testing conditions (Lin et al., for example, found that maintaining a high current density allowed for stable operation under methane [23]), avoiding carbon formation can put severe constraints on the operation of an actual fuel cell application.

Ni/YSZ anodes can also experience problems when operating on syngas. Although carbon formation is not as big a concern as with hydrocarbons, cells operating at low current densities and high CO partial pressures can catalyze carbon formation via the Boudouard reaction (Reaction 1.6) [24]. Jiang and Virkar [25] also showed that nickel is a much better catalyst of H_2 than CO, a fact corroborated by Matsuzaki and Yasuda [26] who found that at 750 ºC the oxidation rate of H_2 is 1.9-2.3 times faster than that of CO. In the same paper, it was demonstrated that for an

electrolyte supported cell with a 25μm anode, performance suffered for $P_{CO}/(P_{CO}+P_{H2})$ ratios greater than 0.2 at 750 ºC under humidified conditions [26]. This was attributed to large diffusion resistances experienced by CO and to a lesser extent, slower CO oxidation kinetics. For $P_{CO}/(P_{CO}+P_{H2})$ ratios below 0.2, however, there was no significant difference in performance when compared with a fuel mixture of H_2 and H_2O. This similarity with humidified H_2 flows indicates the water gas shift reaction tends to convert CO to H_2. Both these phenomena (relatively slow CO oxidation kinetics and syngas flows behaving similar to H_2 flows) have been corroborated by several studies [4, 25, 27].

As Ni/YSZ anodes are prone to carbon deposition when operating on hydrocarbons and also experience performance drops with syngas feeds containing moderate CO concentrations, focus has been directed towards other anode materials. One of the leading candidates is ceria (CeO_2). CeO_2 is a known catalyst and electrocatalyst that has been shown to operate on hydrocarbon fuels without forming carbon [28, 29]. It is also a mixed ionic/electronic conductor that helps extend the active three phase boundary into the anode bulk while doubling as a current conductor. Ceria's electronic conductivity, however, is too low (~0.2 S/cm^2) to be the sole current conductor. In this regard, efforts have been made to add a supplemental material that provides a lower resistance path for exiting electrons.

Copper has been shown to fill this role nicely with numerous studies demonstrating the functionality of Cu-CeO_2 composite anodes operating on H_2 and hydrocarbon fuels [28-30]. Costa-Nunes et al. [4] also studied pure carbon monoxide and dry syngas performance with Cu-CeO_2 cells. It was found that there was little

difference in performance between pure H_2 and pure CO fuels [4]. For syngas, performance was slightly worse than the CO and H_2 cases, but this was attributed to excess dilution with an inert gas rather than a drop in catalytic activity. A Ni/YSZ cell was then tested and compared with the Cu-CeO_2 cell. In this case performance on syngas was slightly worse than performance on H_2, but performance on CO was significantly lower than performance on either H_2 or syngas [4]. These results are to be expected given nickel's poor CO kinetics and the propensity of syngas to undergo water-gas shift reactions.

Copper anodes without CeO_2 have also been explored as a possible anode composition. These anodes however, perform poorly compared with mixed Cu-CeO_2 anodes indicating that copper is a poor electrocatalyst and acts primarily as a current conductor in a composite anode structure [5].

Although Cu-CeO_2 anodes perform well on syngas and hydrocarbons, the use of Cu as a current collector means that a significant amount of space, and therefore TPB length, is occupied by a relatively inactive material. In this regard research has recently turned to Ni/CeO_2 composite anodes. In these anodes, CeO_2 and nickel operate together as oxidation catalysts, with the nickel doubling as a conductor. For direct operation on hydrocarbons and syngas, the CeO_2 reforms the fuels into a more H_2 rich flow. This allows nickel to be present throughout the anode without risk of catalyzing the formation of carbon. It also allows nickel to be present near the electrolyte and thereby contribute as an electrocatalyst.

Early studies indicate that Ni/CeO_2 anodes are a promising anode composition. Qiao et al. [31] incorporated Ni and CeO_2 into a YSZ framework using

a co-impregnation process. Only H_2 fuels were tested, but power densities in excess of 500 mW/cm^2 were obtained. Zhu et al. [14] tested Ni/YSZ anodes impregnated with samaria-doped ceria (SDC) on H_2 and methane fuels at 600 ºC. They showed that the presence of SDC improved performance for both fuels. As SDC is ionically conductive, the performance jump for H_2 is most likely due to the SDC expanding the TPB regions rather than by boosting electrocatalytic activity. For operation on methane, however, the SDC appeared to prevent carbon buildup: cells without SDC experienced precipitous drops in power densities, but those with SDC experienced stable power densities around 350 mW/ cm^2 for 50 hours. Trembly et al. [32] demonstrated stable performance using a Ni/Gadolinium-doped ceria (Ni/GDC) anode with syngas fuels and Suwanwarangkul et al. [24] did the same with Ni/CeO_2 anodes. In addition to functioning well with syngas fuels and methane, Ni/CeO_2 anodes have also been shown to be sulfur tolerant [32, 33].

Although these studies represent a good starting point for understanding Ni/CeO_2 anodes, the research in this area is by no means fully complete. There is room to further corroborate data for performance on hydrocarbons other than methane and in high power density applications using syngas fuels.

1.4 Context and Objectives of This Study

This study looks to develop SOFC architectures that provide high and stable power densities on reformed hydrocarbons. Operation on reformed hydrocarbons was chosen as a starting point for further studies on direct hydrocarbon feeds to

SOFC anodes. The composition of oil well off-gases varies significantly from well to well and can contain high compositions of sulfur [34]. Designing a cell that can operate on a homogenous and predictable reformate stream seems more likely to initially succeed than designing a cell that can operate on a multitude of hydrocarbons in unpredictable ratios.

As it is difficult to simulate any real off-gas mixture and as off-gases can contain significant quantities of C2-C5 hydrocarbons [34], butane (C_4H_{10}) was chosen as a representative species to be reformed. Butane was also selected because many studies have looked into Ni/CeO_2 based anodes for operation on methane or reformed methane, but no known studies have done the same for butane or its reformed products [14, 35-37].

Different anode architectures will be tested with a material focus on Ni/YSZ and Ni/CeO_2/YSZ anodes CeO_2 will be introduced into Ni/YSZ anodes using two different fabrication schemes. The first, called the co-firing method, involves mixing CeO_2 with nickel and YSZ during early stages of fabrication. The second, termed impregnation, involves infiltrating a CeO_2 solution into an existing Ni/YSZ matrix late in the fabrication process. The co-firing scheme is the simpler of the two and allows greater control over cell architecture, but it also involves heating the CeO_2 to temperatures that can significantly reduce its electrocatalytic activity [5]. It is still being pursued as a fabrication method both to verify the drop in electrocatalytic activity and to determine if there is also a drop in reforming activity. The impregnation scheme is slightly more complex and leads to more uncertain cell architectures, but does not expose the CeO_2 to detrimental temperatures.

Performance of Ni/CeO_2/YSZ anodes made with both fabrication schemes will be compared to a baseline Ni/YSZ anode.

This study aims to accomplish the following:

- establish fabrication protocols for high performance Ni/YSZ and Ni/CeO_2/YSZ cells
- operate fabricated cells on syngas streams characteristic of a reformed butane mixture for a steam to carbon ratio of 1.5
- evaluate performance effects of adding CeO_2 to Ni/YSZ cells and determine a preferred fabrication scheme

The following chapters discuss the fabrication, testing, and analysis of different MEA architectures with an emphasis on variation in the anode structure and materials. Chapter 2 describes the development of the fabrication processes and highlights the methods that ultimately led to successful cell designs while detailing many of the difficulties and failures encountered. Chapter 3 describes the experimental setup and the testing preparation and methodology. Chapter 4 and Chapter 5 provide the testing results and analyses for Ni/YSZ anodes and Ni/CeO_2/YSZ anodes respectively. Conclusions and directions for future research are discussed in Chapter 6.

Chapter 2: Fabrication

Several methods were explored for the fabrication of high power density SOFC MEAs. Some of these methods enjoyed varying degrees of success, while others resulted in only non-functional cells. Many of the more promising fabrication schemes closely emulated those described in Armstrong and Rich [9]. Koh et al. [38] was also a valuable source in developing a method for making the electrolyte and Craciun et al. [39] was helpful in developing the protocol for CeO_2 impregnation.

2.1 Cell Geometry

This study utilized an anode-supported geometry. All fabricated anodes were a composite of either Ni/CeO_2/YSZ or Ni/YSZ materials. YSZ was chosen as the electrolyte material for its low electronic conductivity and acceptable ionic conductivity at temperatures near 800 °C. LSM-YSZ was chosen as the composite cathode material because it is a well studied composite that is used in most commercial SOFC development efforts.

The anode was composed of two layers: a thick support layer and a thin functional layer. The support layer was ~1.0 mm thick, porous, and contained different quantities of nickel, YSZ, and CeO_2 depending on the cell being tested. The functional layer was approximately 20 μm thick with a low porosity. YSZ was the material of choice for the electrolyte. Normal electrolyte thicknesses were between 20-25 μm with one cell having a thickness of 10-12 μm. The thinner electrolyte was

used in only one architecture due to difficulties in replicating functional cells with an electrolyte of the reduced thickness. Two cathode architectures were explored. One exploited a two layer geometry that incorporated a functional layer. In this cell the functional layer was approximately 30 μm thick and contained LSM and YSZ. The second layer was a current collector layer approximately 40 μm thick that contained only LSM. The second architecture consisted of just one mixed LSM/YSZ layer 30-50 μm thick. A typical cell geometry for a Ni/YSZ cell utilizing a single layer cathode is shown in Figure 2.1.

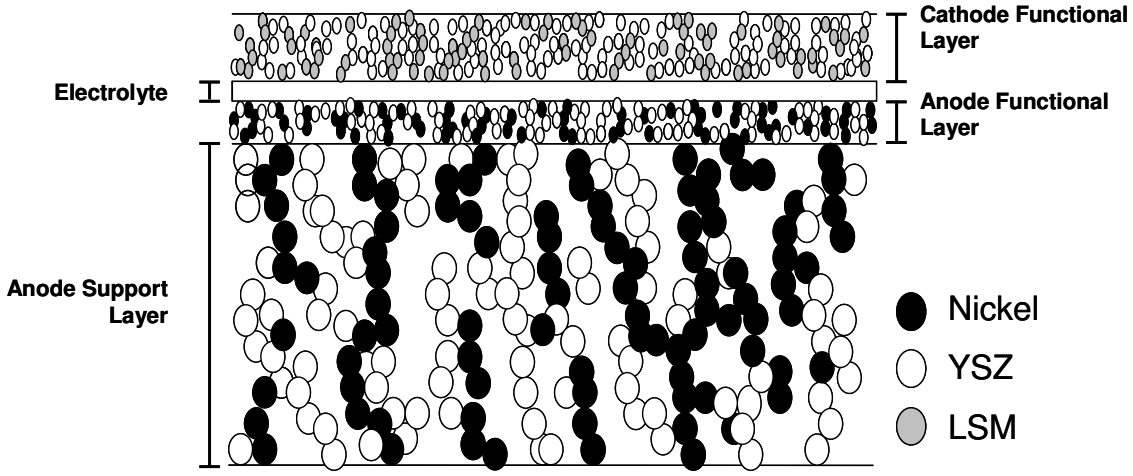

Figure 2.1 Schematic of cell geometry for a Ni/YSZ cell (not to scale)

The baseline cell contained nickel and YSZ in the anode support and functional layers. For the co-fired cells, two microstructures were evaluated. The first microstructure contained CeO_2 in the support layer, but not the functional layer. The second contained CeO_2 in both the support and functional layers. One cell with impregnated CeO_2 was also tested in order to compare the co-fired and impregnation

methods. A scanning electron miscroscope (SEM) image of a typical anode architecture is shown below in Figure 2.2.

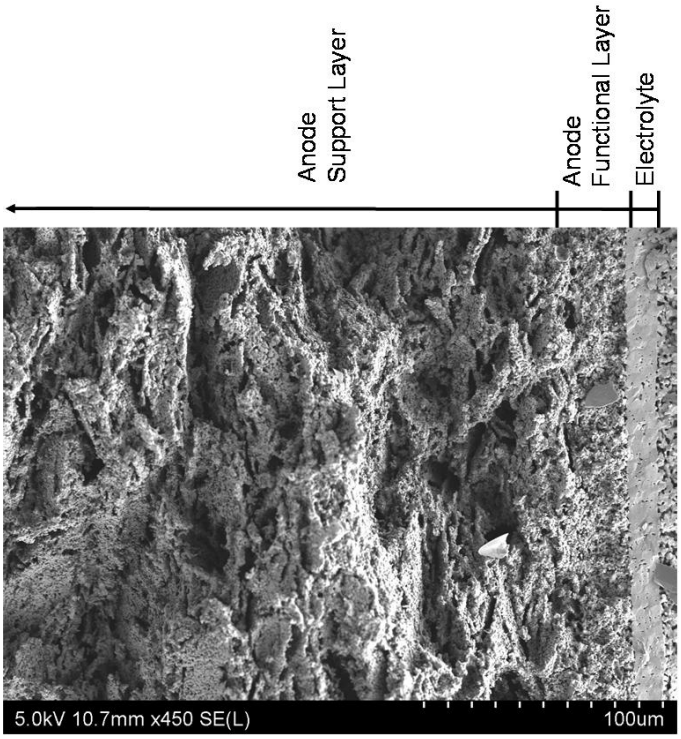

Figure 2.2 Sample anode geometry of a reduced Ni/YSZ cell with the support layer, functional layer, and electrolyte labeled.

2.2 Fabrication of Ni/YSZ Cells

Fabrication began with the anode support layer. 70% wt. Nickel (II) Oxide (*Fisher Scientific*, NiO) and 30% wt YSZ (*Tosoh*, $(Y_2O_3)_{0.08}(ZrO_2)_{0.92}$) were mixed in ethanol to create a slurry. This slurry was ball-mixed for a minimum of 22 hours after which 20% wt. graphite pore former was added (Timcal, 44μm average particle diameter). After a minimum of 2 additional hours of ball-mixing, the mixture was dried under a heat gun for no less than half an hour. The dried powder was passed through a 125 μm sieve to remove agglomerates and then pressed at 9,000 kg of mass

over an approximate area of 6.5 cm^2. This produced a solid pellet. The pellet was then placed in a furnace and heated to 900 ºC at a rate of 1.5 ºC/min. The cell was kept at 900 ºC for 3 hours and then cooled at a rate of 1.5 ºC/min. This heating was performed to burn out the graphite pore former and produce a porous NiO/YSZ matrix. Porous alumina plates were placed on top of the cell during heat up to prevent curling. It was found that 3-4 plates (~18-24 g) provided adequate pressure to prevent curling while not flattening the cell.

A low porosity NiO/YSZ functional layer was then added to the support layer. The powder for the functional layer was created in an analogous manner to that for the support layer only with a NiO:YSZ ratio of 6:4 instead of 7:3. As the desired porosity was ultimately generated by NiO reduction to Ni, graphite pore former was not added. After drying and sieving, the powder was ultrasonically dispersed in isopropanol for five minutes. As NiO and YSZ do not dissolve in isopropanol, a small quantity of polyvinyl-butyral (PVB) was added to enhance uniformity and slow particle settling. This was followed by further sonication lasting a minimum of 30 minutes. A known quantity of the suspension was then pipetted onto the surface of the anode and left to air dry for 20 minutes. This created a thin, uniform NiO/YSZ functional layer.

This process of pipetting the suspension onto the support layer is known as drop coating. It is a fairly simple process that gives surprisingly good results. The difficult part is not in the process, however, but in the development of the proper suspension. If the suspension has an improper viscosity, surface tension, or volatility then problems such as poor dispersion and/or non-uniform coverage can result.

Having the suspension wick into the porous substrate instead of drying on top is another problem. These problems can be overcome through proper selection of solvent and dispersant. Care also needs to be taken to mix the solvent, dispersant, and powder in appropriate ratios. Initial ratios were taken from Koh et al. [38] and adjusted as needed to give the best results. The appropriate quantities of powder, solvent, and dispersant are given in Table 2.1 for the functional layer and electrolyte, which was also drop-coated (these ratios were the same for all fabricated cells except for *Cell 2* which used slightly less YSZ in the electrolyte than the other three cells). The corresponding layer thicknesses for the given quantities are also provided. After the addition of the functional layer, the cell was again heated to 900 ºC using the same cycle as before. This cycle was executed to burnout any undesirable remnants of the drop coating process.

Table 2.1 Suspension composition used for drop-coating the functional layer and electrolyte. Quantities listed are for one cell.

	Isopropanol (μL)	Powder (g)	PVB (g)	Final Thickness (μm)
Functional Layer	700	0.06	0.01	20-25 μm
Electrolyte*	700	0.06	0.015	20-25 μm

* 0.03 g YSZ were used to fabricate the electrolyte for *Cell 2* resulting in a 10-12μm thickness

The appropriate ratios of solvent, powder, and PVB for the electrolyte were determined in a similar manner as the ratios for the functional layer. YSZ and PVB were first added to the isopropanol. The suspension was then sonicated for 30 minutes. The suspension was then drop-coated onto the functional layer and the cell

heated to 1400 ºC at a rate of 1 ºC/min. The cell was kept at 1400 ºC for 3 hours and then cooled at 1 ºC/min. This heat cycle was expected to eliminate pores in the electrolyte and ensure proper sintering between the functional layer and the electrolyte. The heating also resulted in the cell shrinking to approximately 80% of its original diameter. As the electrolyte tended to shrink more than the anode, cells without proper weighting became concave when viewed with the electrolyte facing up. In order to prevent this, two alumina plates and two zirconia plates (total weight ~30-35 g) were stacked on top of the cell with one of the alumina plates placed directly on top of the electrolyte (it was found that zirconia plates tended to stick to the electrolyte). As nickel-oxide reacts with alumina at these temperatures, cells were also placed NiO side down on top of zirconia plates.

The cathode was added as a final step. The cathode was fabricated from a 50/50% wt. $(La_{0.80}\ Sr_{0.20})$ Mn 0_{3-x}/YSZ (LSM/YSZ) composite paste purchased from *Fuel Cell Materials*. To increase porosity, the paste was attritor milled for three minutes with 10% wt. graphite pore former (*Timcal*, 4 μm average particle diameter). Isopropanol (~150 μL per 1 g of paste) was also added to decrease viscosity. The paste was then slurry cast over a 0.95 cm diameter circular mask made from Kapton tape (*Kaptontap.com*, 2 mil thick tape). After drying the cathodes under a heat gun for 10-15 min. the mask was removed. The cells were then heated to 1300 ºC over the course of 2,200 min. This heating was necessary to sinter the cathode to the electrolyte. Final cathode thicknesses varied between 30 and 50 microns. This range in thicknesses was due to repeatability issues with the slurry casting process. As a

final step the cell anode was exposed to a H_2 rich environment to reduce the NiO to Ni.

This completes the fabrication of a Ni/YSZ cell. A picture of an unreduced cell is shown in Figure 2.3. The cathode is the black dot in the middle of the cell. The electrolyte extends to the edge of the cell, but as it is transparent, the green unreduced NiO/YSZ anode is visible. When the NiO is reduced to Ni, the anode color changes from green to grey. The active geometric area of the cell is estimated by the area of the cathode, which is the limiting area and only a fraction of the anode and electrolyte area.

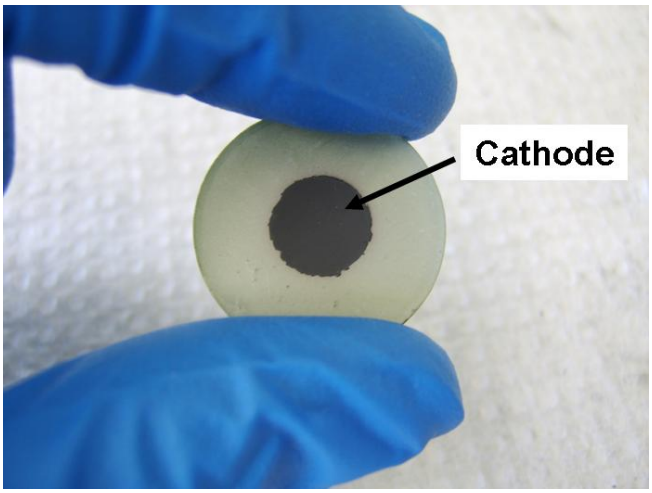

Figure 2.3 Image of a fully fabricated but unreduced cell. The electrolyte is transparent making only the cathode and the anode visible.

2.3 Fabrication of Ni/YSZ/CeO_2 Cells

Two methods were used to introduce CeO_2 into the anodes. The first called co-firing, introduced CeO_2 into the anode early in the fabrication process. Co-firing was a simple process that resulted in exposing the CeO_2 to the high temperatures

needed to sinter the electrolyte and cathode. The second method, called impregnation introduced the CeO_2 as a final fabrication step, thereby avoiding the high temperature exposure.

Two cells (*Cell 2 and Cell 3*) were fabricated using the co-firing method, both of which were fabricated in a near identical manner as *Cell 1*. One difference, however, was that NiO, YSZ, and CeO_2 were ball-mixed together to create the support layer powder instead of just NiO and YSZ. For *Cell 3* CeO_2 was also added to the NiO and YSZ powders used to make the functional layer. The functional layer in this case was composed of 50% wt NiO, 30% wt YSZ, and 20% wt CeO_2. For *Cell 3*, all other fabrication steps were the same as that for the Ni/YSZ cell. For *Cell 2* an additional LSM current collecting layer was slurry cast on top of the LSM/YSZ cathode layer. All other steps were the same. SEM images of the functional and support layers of *Cell 2* are shown below at two different magnifications.

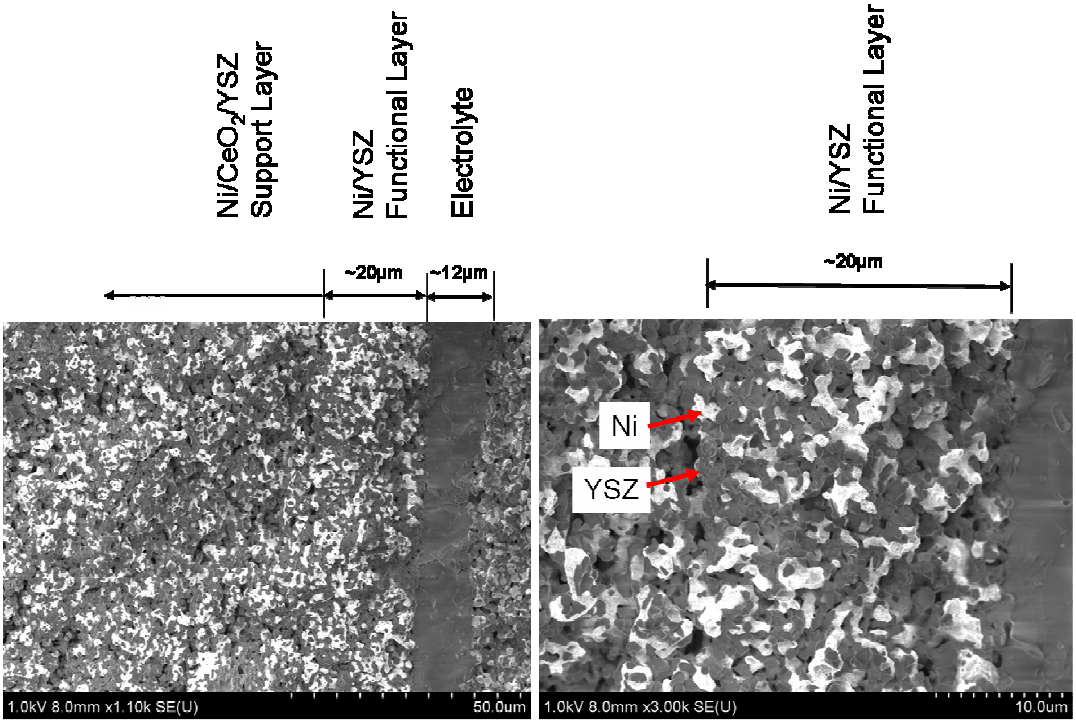

(a) (b)

Figure 2.4 SEM images of the *Cell 2* anode microstructure. The bright particles are Ni and the dark particles are YSZ. (a) 1100x magnification (b) 3000x magnification

Fabrication of the CeO_2 impregnated cell was also very similar to that of the Ni/YSZ cell. One difference was that 25% wt. graphite pore former was added to the NiO/YSZ mixture during ball-mixing instead of 20% wt. This was done to generate an enhanced pore structure for the CeO_2 impregnation process. This added pore former weakened the cell slightly, making it necessary to reduce the weight applied during the electrolyte cycle from 30-35 g to 25-30 g. The fabrication then remained the same through the sintering of the cathode.

After sintering the cathode, the cell was impregnated with CeO_2. The impregnation process began with dissolving $Ce(NO_3)_3 \cdot 6H_2O$ (*Strem Chemicals*) in water and 1-propanol. The solution was sonicated for 10-15 min. to accelerate the

dissolution process. The propanol was added to reduce the surface tension and allow for improved infiltration. It was found that 1 g of $Ce(NO_3)_3 \cdot 6H_2O$ dissolved in 550 μL of water and 140 μL of propanol created a solution with an acceptable surface tension. This solution was pipetted onto the anode surface in small quantities (20-40 μL) and allowed to infiltrate into the porous cell. As the solution tended to penetrate the entire depth of the anode, CeO_2 made its way into the functional layer in addition to the support layer. Once saturated the cell was heated to 500 ºC in air to decompose the nitrates and produce CeO_2 [5]. This nitrate decomposition led to the formation of additional void spaces, allowing for further CeO_2 impregnation. The process of impregnation followed by heating was repeated until the desired amount of CeO_2 was introduced into the cell. For this study one heating cycle was sufficient to reach the desired CeO_2 content.

This completed fabrication of the different cells. Table 2.2 summarizes the microstructure and composition of all cells. The porosities were estimated by first measuring the volume of a fully fabricated anode. Given this volume, the porosity could then be determined given the known mass and density of each material present in the anode.

Table 2.2 Basic microstructure summary of tested micro-architectures

	Cell Parameter	Cell 1	Cell 2	Cell 3	Cell 4*
Anode Support Layer	Wt. % NiO	70	65	65	70
	Wt.% YSZ	30	25	25	30
	Wt. % CeO_2	0	10	10	?
	Calculated Porosity (%)	61	61	61	61
Anode Functional Layer	Wt. % NiO	60	70	50	60
	Wt.% YSZ	40	30	30	40
	Wt. % CeO_2	0	0	20	?
	Calculated Porosity (%)	23	28	31	23
Electrolyte	Thickness (μm)	20-25	10-12	20-25	20-25
Cathode Functional Layer	Calculated Porosity (%)	0.26	0.26	0.26	0.26
Cathode Current Collecting Layer	Calculated Porosity (%)	-	0.27	-	-

* CeO_2 contents in the functional and support layers were unknown, but the total amount added was 5% of the total unreduced anode weight. NiO percentage is given as a weight percentage prior to CeO_2 impregnation.

Chapter 3: Experimental Setup

The solid oxide fuel cells in this study were tested in a rig designed to withstand the elevated temperatures of SOFC operation. Cells were mounted on cast alumina tubes and placed inside a clamshell furnace capable of heating to temperatures in excess of 800 °C. Normal testing temperatures were between 700 and 800 °C. These temperatures made seemingly straightforward issues such as mounting and sealing the cell to the tube difficult. Special care for example had to be given to minimize CTE mismatches between the cell, the tube, and the sealing material. As the leads had to be resistant to oxidizing and reducing atmospheres while at the same time capable of functioning at temperatures around 800 °C, special consideration was also needed for attaching the leads to the electrodes. A series of mass flow controllers were setup to deliver air and fuel to the cathode and anode respectively. Electrochemical testing was then performed to gain insight into the cell performance and fundamental behavior.

3.1 Cell Wiring and Sealing

Two different methods for sealing the cell were explored. The first utilized an Al_2O_3 paste to seal around the cell and was used for *Cell 2*. The second utilized a compression based mechanism and was used for *Cells 1, 3,* and *4*. The ceramic paste method was initially explored as an option, but consistently led to cell cracking, *Cell 2* being an exception. These failures are thought to have occurred due to a CTE

mismatch between the cell, heavily loaded with nickel (CTE ~ 18.0 x 10^{-6} ºC), and the paste (CTE = 7.7 x 10^{-6}). A compression based method using mica and glass gaskets was also explored to reduce mechanical stress on the cell. Although more time consuming, the compression-based method proved to be the more repeatable of the two.

3.1.1 Ceramic Paste Sealant

For sealing with the ceramic paste, current-collecting silver wires (12 cm long, 0.5 mm in diameter) were initially spot-welded to a silver mesh (50 mesh, Alfa Aesar). The lead was then threaded through Al_2O_3 tubing (Omega Engineering), which provided thermal insulation and prevented shorts with other wires. The free end of the wire was then wound around a 1 mm diameter silver lead already encased in Al_2O_3 tubing. The mesh (with wire attached) was then pasted onto the cathode using silver paste (Fuel Cell Materials) and dried under a heat gun for 30 min. During dry-out, pressure was applied to the corners of the mesh to ensure a strong bond with the cell (see Figure 3.1). Once dry, a dab of Al_2O_3 paste (Ceramabond 552-VFG, Aremco) was used to further secure the mesh/wire assembly to the cell surface. This paste was allowed to dry for 30 min. In order to further secure the connection between wires, silver paste was applied to the 0.5 mm/1.0 mm windings and dried under a heat gun for 15 min. The cell was then flipped over and an identical process performed for the anode.

Figure 3.1 *A*ttaching the current collecting mesh to the cathode

The 0.5 mm/1.0 mm wire assembly was used because the 1 mm wire by itself was too heavy and rigid when used in isolation and often lead to mesh de-lamination. The 0.5 mm wire, however, was able to flex and thereby reduce forces that tended to pull the mesh from the MEA. As the total length of the 0.5 mm wire was but a couple of inches it was found that η_{ohm} was not significantly affected by its use.

After the anode side mesh was attached, the cell was attached to the end of an alumina tube (*AC Technologies, Cast Alumina Tubes*) using several layers of Al_2O_3 paste. The paste was allowed to dry for 30 min before moving the assembly to the testing rig.

3.1.2 The Compression Method

Wiring again began with the cathode side. One end of a 0.5 mm diameter silver wire was first flattened under 4,500 kg of weight. As will shortly be explained,

this was done to allow for better sealing. The flattened end was then spot welded to a silver mesh slightly larger than the size of the cathode (50 mesh, Alfa Aesar). The non-flattened end was wound around a 1 mm diameter silver wire already encased in Al_2O_3 tubes. The rest of the cathode wiring process proceeded in an identical manner as that described in *Section 3.1.1*.

Before wiring up the anode side, a seal was attached to the cathode side of the cell. The seal consisted of a three layer assembly composed of a single mica gasket (McMaster-Carr) sandwiched between two borosilicate glass gaskets (Advantec MFS*)*. Using the Al_2O_3 paste, the gaskets were first pasted to each other and then to the cell. Gaps between the seal and cell were minimized by the flattened lead. At operating temperatures the glass melted and created an airtight seal. The mica prevented the cell from sticking to the alumina tubes that would eventually hold the cell in place. All gaskets had an outer diameter of 2.5 cm and an inner diameter of 1.6 cm. A simple diagram showing the multi-layered seals on both the cathode and anode sides is shown in Figure 3.2.

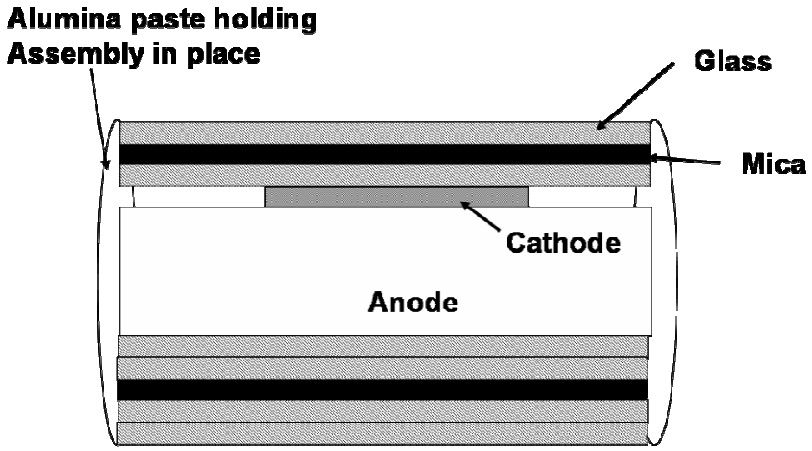

Figure 3.2 Cross sectional view of a cell being sealed by the compression method. The cell is sandwiched between layers of glass and mica. The assembly is held in place by alumina paste.

The cell was then flipped upside down and the seal for the anode side constructed. The seal consisted of the same glass/mica materials as the cathode seal but had two glass gaskets on either side of the mica instead of one. The gaskets were again pasted to each other and the cell. Paste was also used to attach the cathode and anode gaskets to each other. A picture of the cell after both gaskets have been added is shown in Figure 3.3.

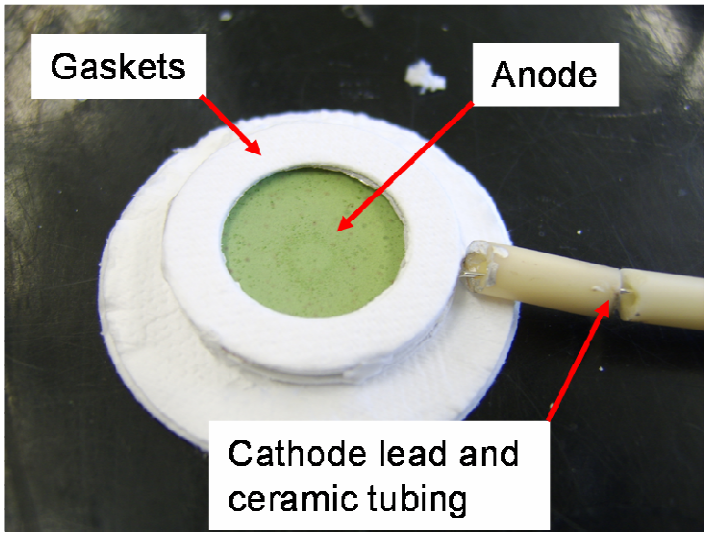

Figure 3.3 Anode side of cell with sealing gaskets attached

Wiring for the anode began with spot welding a 0.5 mm silver wire to a silver mesh about the size of the cathode. The 0.5 mm wire was then wound around a 1 mm wire in an analogous manner to what was done for the cathode lead. Silver paste was applied to the windings and dried under a heat gun for 10 min. The wiring and mesh were then fed through a cast alumina tube. The tube and wire were then vertically oriented and placed above the anode surface of the cell. The wire was then lowered down until the mesh, bent at a 90º angle, laid flat across the cell. The mesh was then pasted to the cell using the same methods used for pasting the cathode mesh. After drying, Al_2O_3 paste was applied to the wire to further secure it to the cell.

3.2 Experimental Rig and Mass Flow Controllers

Before moving the cell/tube assembly into the testing apparatus, a cast alumina tube was inserted inside the existing alumina tube (AC Technologies). This

tube supplied fuel to the cell surface. A rubber stopper attached at one end of the inner tube was wedged into the outer tube to create a seal and keep the inner tube in place. An additional Teflon tube (1/8" OD - Swagelok) was fed through the stopper to allow gases to escape from the anode side tube chamber. A similar arrangement was utilized to deliver air to the cathode.

A test rig that could support a clamshell furnace and properly align the air and fuel tubes was designed and built. A picture of the rig is shown in Figure 3.4. The rig consisted of a rectangular outer frame made from machined aluminum guide rails (TSlots, Futura Industries) with cross members near the bottom that supported the furnace. Tube clamps were attached to two additional cross members, one located near the bottom of the rig and one near the top. The top clamp held the outer tube/inner tube assembly for the cathode while the bottom clamp did the same for the anode. For compression sealing, the upper tube was lowered down on top of the lower tube. It was found that the upper tube assembly provided sufficient compressive weight on its own to form an adequate seal. For ceramic paste sealing, the tubes were placed to within 1 cm of each other.

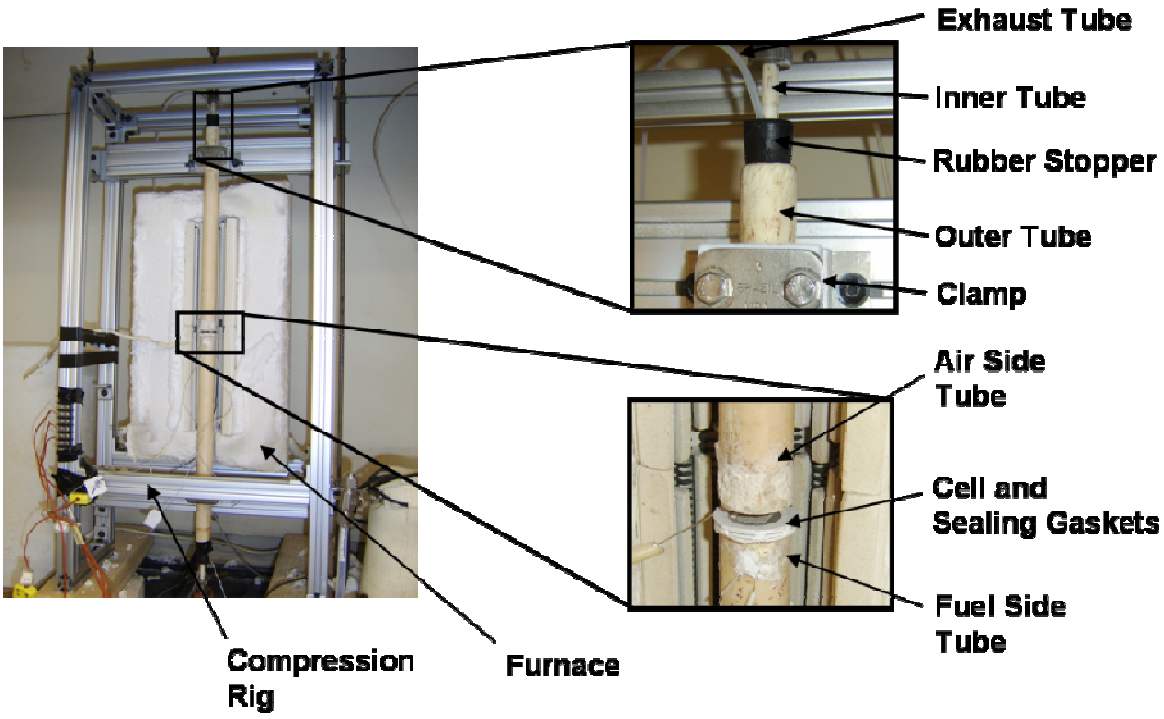

Figure 3.4 Picture of experimental rig. Only half of clamshell furnace is shown.

Two K-type thermocouples were placed inside the furnace. One was used to control the heating and cooling of the furnace (TC1), the other (TC2) was used as a temperature check and for identifying temperature fluctuations characteristic of gas leaks. TC1 was pasted on the fuel side tube, just below the cell. TC2 was left free between the anode tube and heating element. Temperatures determined from TC1 are the reported temperatures in this study. The thermocouple wires were insulated with similar ceramic tubing as the electrical leads, but of a smaller diameter.

On the anode side, H_2, Ar, CO, and CO_2 were directed from compressed cylinders through individual mass flow controllers (MFCs). H_2O could also be added by routing the flow through a humidifier that used heated Nafion tubes (Fuel Cell Technologies). The amount of H_2O added to the stream depended only on the user controlled humidifier temperature. On the cathode side, only one MFC was needed to

control the flow of air which was used as the cathode flow for all experiments. A basic schematic of the experimental setup is shown in Figure 3.5.

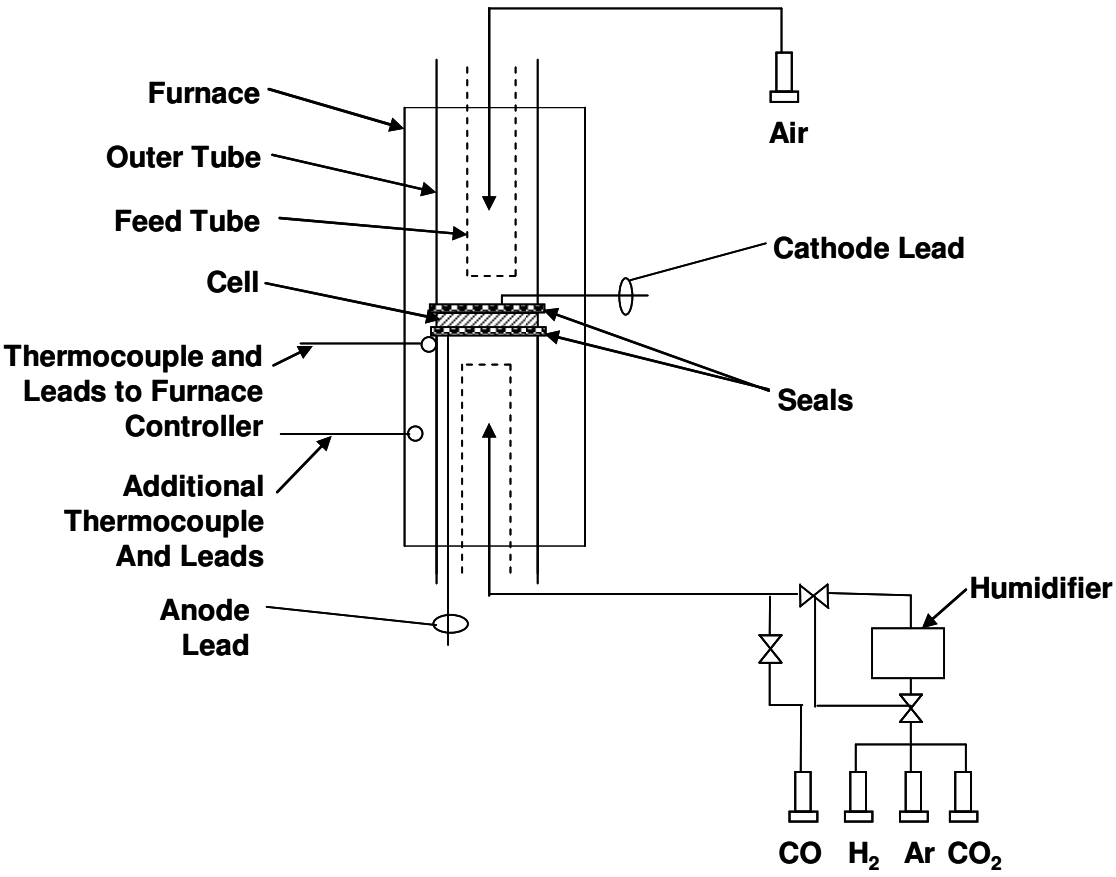

Figure 3.5 Schematic of single cell test rig and MFCs. Compression sealing mechanism shown.

Signals to and from the MFCs and signals from TC2 were routed to data acquisition (DAQ) boards (National Instruments). These DAQ boards interfaced with a desktop computer and its Labview (National Instruments) software to allow for control over gas flow rates. Cathode and anode leads were connected to a *PGSTAT30* Autolab electrochemical work bench (Eco-Chemie). The *PGSTAT30* was hooked up to a 10 Amp current booster (Eco-Chemie) to allow for MEA currents up to 10A.

3.3 Electrochemical Methods

For this study, the Autolab was utilized in a potentiostatic mode for all measurements including linear sweep voltammetry (LSV) and electrochemical impedance spectroscopy (EIS). EIS measurements were performed at a range of DC potentials usually determined by the voltage drop relative to the open-circuit voltage. Both the LSV and EIS tests were used to evaluate cell performance and to gain insight into the fundamental processes that determine cell behavior.

3.3.1 Linear Sweep Voltammetry

The LSV measurements were performed from open-circuit voltage (typically ranging from 0.85 to 1.0 V) down to 0.3 V. 0.3 V was chosen as the lower voltage limit because exposing the cells to lower voltages risked damaging the cells. The voltage and the corresponding currents were plotted against one another to generate a V-I curve. To get a better sense of cell performance, the output power (voltage times the current) was also plotted on the same graph.

As was discussed in *Section 1.2.4*, the shape of the V-I curve often indicates which overpotentials are dominant at which currents. Fitting the V-I data to the overpotential equations (*Section 1.2.4*) allows for the estimation of fundamental cell parameters such as the exchange current density and the effective diffusion

coefficient. The power density data provides a simple graphic of cell performance. Sample V-I curves are shown in Figure 3.6.

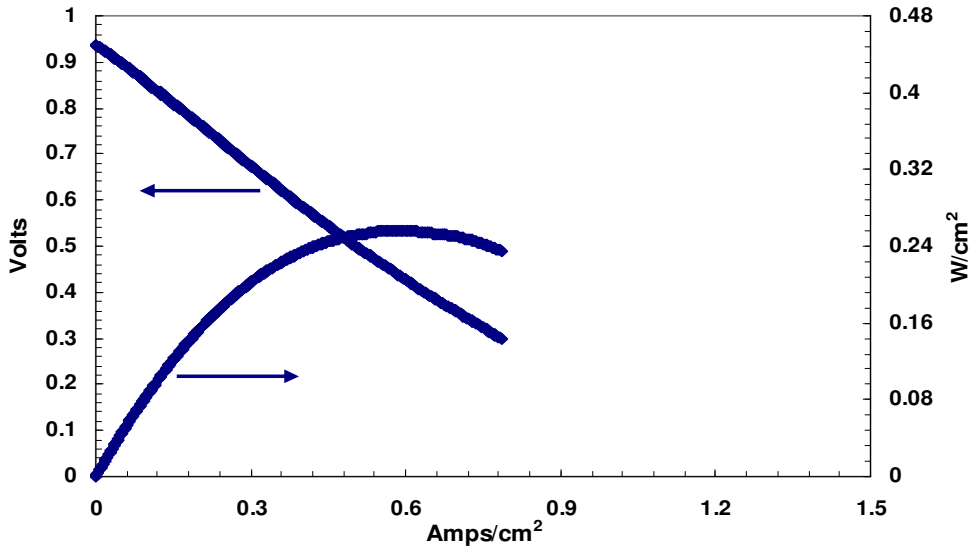

Figure 3.6 Sample V-I curves

3.3.2 Electrochemical Impedance Spectroscopy (EIS)

EIS testing consists of measuring the complex impedance of a cell over a range of voltage frequencies. Using Euler's Formula to express the sinusoidal voltage and current signals, the impedance Z can be expressed as follows where Z_0 is the ratio between the voltage and current amplitudes and ϕ is the phase difference between signals.

$$Z = Z_0\left(\cos(\phi) + i\sin(\phi)\right) \qquad \text{Eq. 3.1}$$

The magnitude of the real component of the impedance is the electrical resistance and the magnitude of the imaginary component is the reactance. If the impedance only has a real component than the current instantaneously responds to the voltage. If the impedance only has an imaginary component, the resistance is zero and the current lags or leads the voltage by 90º. For SOFCs, the impedance always has a real component and for most frequencies also has an imaginary component. By plotting the real component against the imaginary component for a range of voltage frequencies an impedance curve can be generated. An example of an impedance curve is shown in Figure 3.7. Note that the high frequencies are on the left, the low frequencies on the right, and that the y-axis is negative. A negative imaginary component indicates the current lags behind the voltage. As the current normally lags behind the voltage for SOFCs it is convention to plot the negative of the imaginary component instead of the actual value.

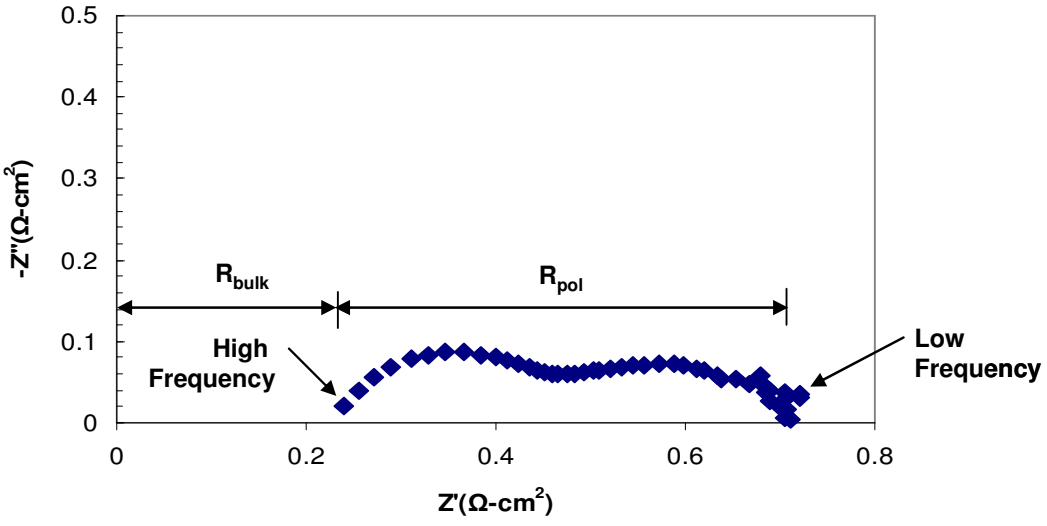

Figure 3.7 Sample impedance curve

EIS testing is a valuable tool because SOFC processes have a wide range of characteristic frequencies. Electron and O^{2-} ion conduction are very fast and as such provide the real impedance (R_{ohm} or R_{bulk}) at the highest frequencies. Thus, the high frequency intercept with the x-axis is a purely resistive R_{bulk} that is equated to R_{ohm}. As the frequency is decreased from the high value of 10 kHz, the electrochemical and surface chemistry processes begin to impede current flow by both allowing charge to flow and to build up at the phase interfaces where charge transfer takes place.

The low frequency intercept is therefore like the total resistance which includes the high frequency R_{ohm} and all resistances associated with surface chemistry, transport, and charge transfer processes. These additional resistances are often referred to as the polarization resistance, R_{pol}.

As the impedance is highly dependent on cell microstructure and testing conditions, it is difficult to definitively assign processes to certain frequencies or curve features. Some processes, however, can be associated with a range of frequencies. Charge transfer processes, for example, normally respond to high frequencies near 10 kHz while gas diffusion processes normally respond to lower frequencies [40]. The exact range of frequencies for diffusion processes is difficult to isolate, but Primdahl and Mogensen found that diffusion processes in a Ni/YSZ cell could be attributed to frequencies between 10 and 100 Hz [41].

Insight from the impedance curves can be gained by changing the gas composition over one electrode while keeping it constant over the other. This is because the electrolyte behavior in SOFCs is largely independent of electrode conditions. Any resulting change in shape in the impedance curve can then be

attributed to the electrode experiencing the changing compositions. Varying the constant DC voltage about which the signal oscillates can also lead to changes in the impedance curve. Comparing impedance curves at very high overpotentials where transport losses become significant with impedance curves at very low overpotentials where activation losses are more significant, for example, can indicate frequencies over which gas diffusion or activation processes are most important. Other tests can also be performed on a case by case basis and it is often up to the experimenter to determine what tests will provide the most useful information about a given cell.

3.4.2 Testing Conditions

Cells were heated up to 800 ºC at a rate of 1 ºC/min. During this time air was flown on the cathode side and H_2 diluted in Ar on the anode side. Once at temperature, the flow was changed over the course of an hour to P_{H2} = 48.5 bar, P_{Ar} = 48.5 bar, and P_{H2O} = 0.03 bar. The H_2 flow was also increased from 10 to 200 sccm over this period. The cell was exposed to this flow for several hours to reduce the NiO to Ni and to ensure a stable OCV prior to testing.

LSV and EIS tests were performed for several gas compositions and for temperatures ranging from 700 to 800 ºC. The cells were first exposed to different anode gas compositions at 800 ºC. These compositions included H_2 flows for a range of water contents and syngas flows of varying compositions (see Table 3.1). The changing syngas compositions were reflective of how the fuel composition would evolve as it flowed down the channel in a planar SOFC anode. At the entrance of a parallel flow cell (0% conversion, labeled $S_{0\%}$) the flow is fuel rich while in the

middle of the cell (50% conversion, labeled $S_{50\%}$) the flow contains significantly more product species. On the cathode side, the flow of air was kept constant.

Table 3.1 Tested gas compositions for the cells reported in this study.

		Partial Pressures					H_2 Flow
		P_{H2O}	P_{H2}	P_{Ar}	P_{CO}	P_{CO2}	(sccm)
Humidified H_2 Compositions	Flow 1	0.03	0.485	0.485	0	0	200
	Flow 2	0.15	0.425	0.425	0	0	200
	Flow 3	0.30	0.35	0.35	0	0	200
Syngas Compositions	0% Conversion ($S_{0\%}$)	0.651	0.082	0	0.215	0.051	200
	25% Conversion ($S_{25\%}$)	0.499	0.234	0	0.151	0.116	200
	50% Conversion ($S_{50\%}$)	0.328	0.405	0	0.105	0.162	100

For all flows at 800 °C at least two LSV tests were performed as well as EIS tests at 100 and 300mV overpotentials. At least two LSV tests were then performed at 750 ºC for the $S_{0\%}$ syngas composition. The temperature was then reduced further to 700 ºC and the cell tested on all three syngas compositions. Here at least two LSV tests were performed in addition to EIS tests at 100 and 300mV overpotentials. *Cells 3* and *4* experienced an unexpected failure after testing at 800 ºC and were not tested at the lower temperatures.

Upon completion of testing, the cell was cooled down at a rate of 1 ºC/min. Air was flown on the cathode side and a dilute H_2 mixture was flown on the anode side. H_2 was flown during cool down to ensure nickel remained in its reduced form. The apparatus was then inspected for faulty seals, proper tube alignment, and cell

cracking. The cell was then removed and the microstructure explored using a Hitachi SU-70 scanning electron microscope (SEM). Additionally, elemental composition was characterized using energy-dispersive X-ray spectroscopy (EDS, *Bruker XFlash Silicon Drift Detector*). This was done to verify that the proper materials were in the proper locations.

Chapter 4: Ni/YSZ Anode Performance

4.1 Hydrogen Testing and Analysis

A Ni/YSZ cell (*Cell 1*) was tested to generate a baseline case for performance without CeO_2. This was done to clearly determine the impact CeO_2 may have on anode performance. It was also important to test a Ni/YSZ cell on syngas fuels to determine if any resulting degradation in performance occurred due to carbon formation.

V-I curves for several humidified H_2 flows at 800 ºC are shown below in Figure 4.1. The least humidified anode flow with $P_{H2} = 0.485$ bar and $P_{H2O} = 0.03$ bar, had a slightly higher maximum power density with a value of 0.26 W/cm^2 while the flows with $P_{H2O} = 0.15$ and 0.30 bar both had maximum power densities of 0.25 W/cm^2. It was thought that higher P_{H2O} would lead to larger anode concentration overpotentials $\eta_{conc,a}$ at high current densities and cause a decrease in V_{cell}. At $P_{H2O} =$ 0.30 bar, however, the concentration overpotential did not appear to be larger than at $P_{H2O} = 0.03$, and the flows performed the same.

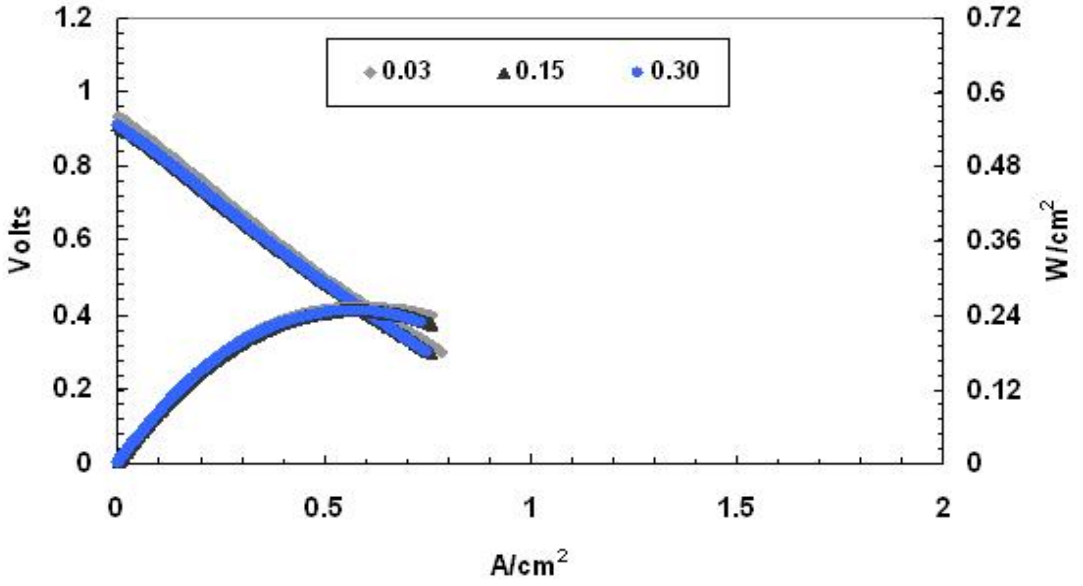

Figure 4.1 V-I curves at 800 ºC for H_2 flows with P_{H2O} = 0.03, 0.15, and 0.30 bar.

The OCVs for all three curves were below the thermodynamically predicted values. The thermodynamic OCVs for H_2 flows with P_{H2O} = 0.03, 0.15, and 0.30 bar are 1.07, 0.99, and 0.95 V respectively while the measured OCVs were 0.94, 0.91, and 0.90 V respectively. The lower OCVs are likely due to gas leakages across the electrolyte and not electronic conduction in the electrolyte membrane. Electronic conduction seemed unlikely given YSZ's very low electronic conductivity at these temperatures. Gas leaks through pinholes in the electrolyte, however, reduce P_{H2} and increase P_{H2O} in the anode and cause a drop in the OCV based on Equation 1.3. Visual inspection after testing revealed that the seal remained intact and well adhered to the cell, but this does not eliminate the possibility of non-visible leaks due to a faulty seal as an explanation for a reduced OCV. SEM images taken of the electrolyte, on the other hand, show the existence of many pores (Figure 4-2).

Although these pores do not always appear contiguous, their prevalence lends credence to the pin-hole explanation.

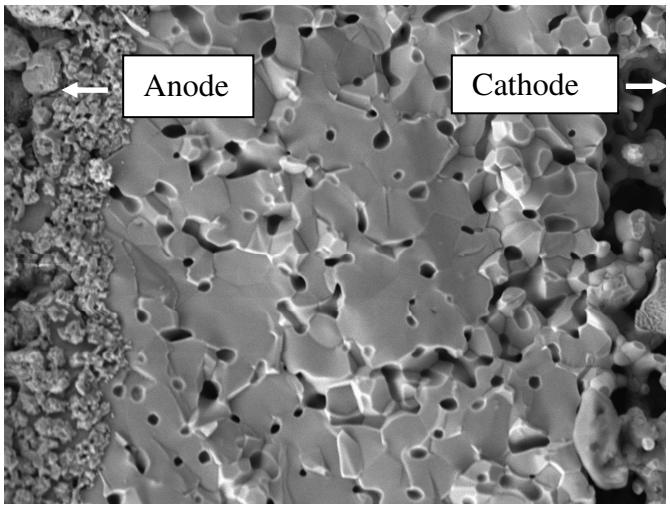

Figure 4.2 SEM image of the electrolyte for *Cell 1*

Impedance spectra at η_{tot} = 300mV (~0.15 A/cm^2) for different P_{H2O} are shown in Figure 4.3. An additional curve for P_{H2O} = 0.03 at η_{tot} = 100mV (~0.15 A/cm^2) is also shown. At η_{tot} = 300mV, the high frequency intercept occurs at R_{ohm} = 0.33 Ω•cm^2 and the low frequency intercept occurs between 0.95 Ω•cm^2 and 1.0 Ω•cm^2 implying a total $R_{pol} \approx$ 0.65 Ω•cm^2. Given the near constant slope of the different V-I curves, it is not surprising that the impedance curves are quite similar for the different P_{H2O}.

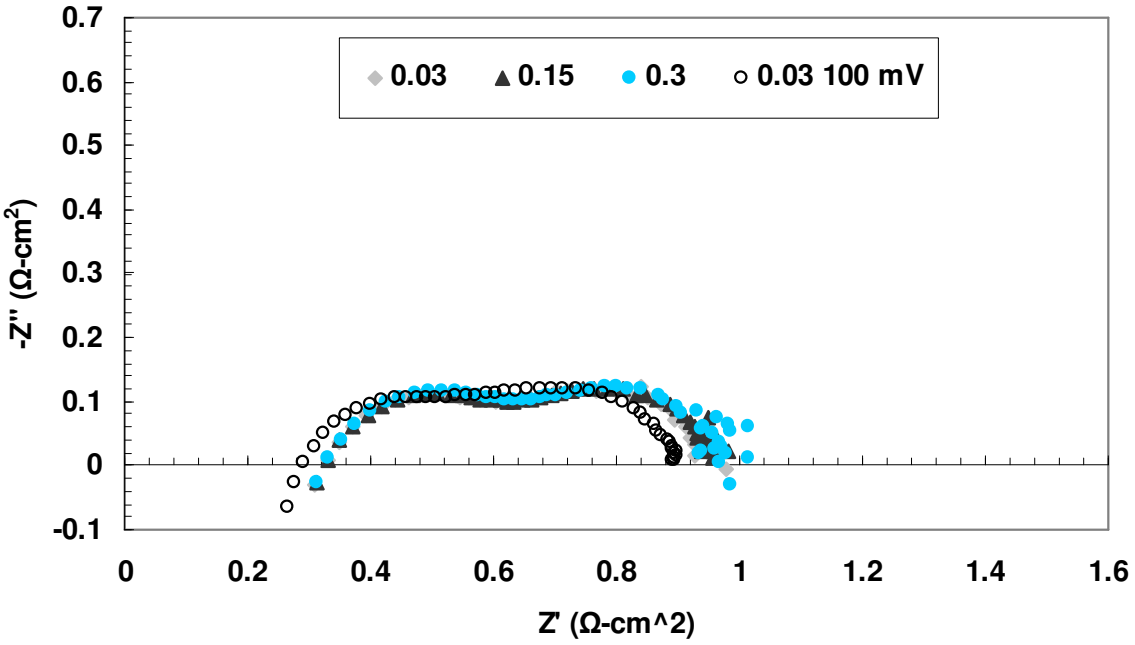

Figure 4.3 Impedance spectra at 800 ºC for a range of P_{H2O}

Comparing the η_{tot} = 100mV and η_{tot} = 300mV cases in Figure 4.3 reveals that R_{ohm} (signified by the high frequency intercept) increases slightly from 0.29 Ω·cm^2 at η_{tot} = 100mV to 0.32 at η_{tot} = 300mV. This increase in R_{ohm} with η_{tot} (or current density i) was observed to some degree for all tested cells. At high current densities oxygen ions travel further distances through the anode or cathode bulk and this increases R_{ohm} [42].

4.2 Syngas Testing

The V-I curves for the syngas flow $S_{0\%}$ at 800 ºC are compared with the H_2 data with P_{H2O} = 0.15 bar in Figure 4.4a. The two V-I curves are nearly identical as are the maximum power densities: 0.26 W/cm^2 for the syngas flow and 0.25 W/cm^2 for the H_2 flow. This similarity between the different fuels is likely caused by the

excess H_2 in the flow dominating the electrochemical reactions. Also at these temperatures CO and H_2O were likely shifted into H_2 and CO_2 (Reaction 1.5) and as a result CO probably did not significantly impact the electrochemical reactions [4].

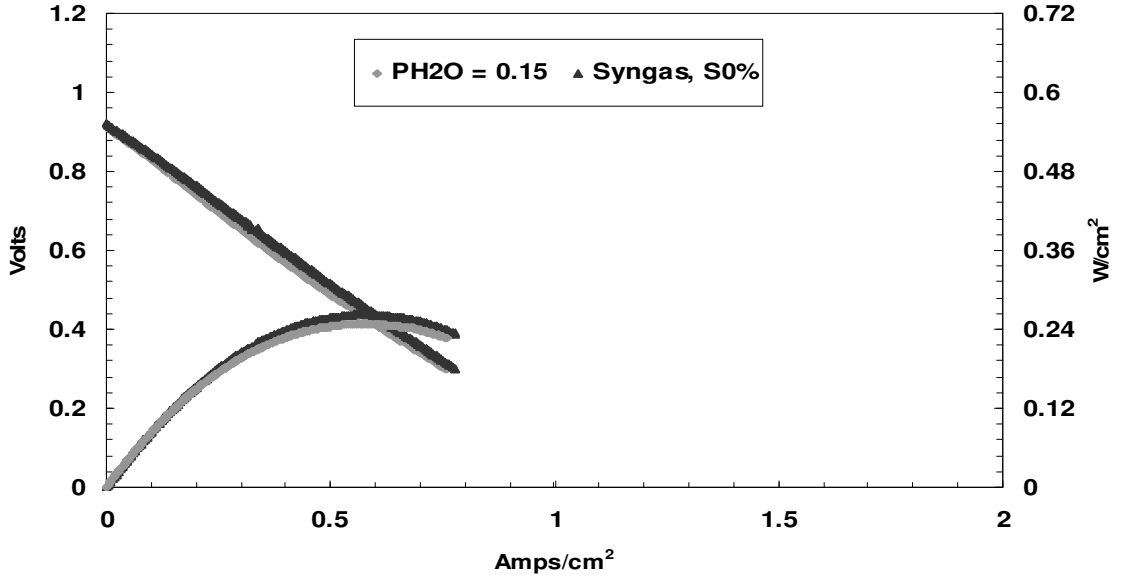

(a)

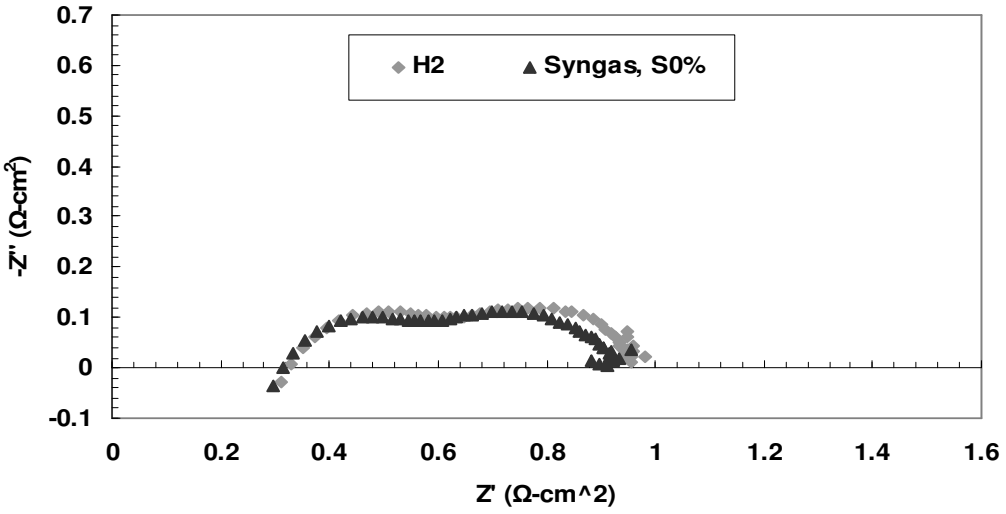

(b)

Figure 4.4 Comparison of H_2 (P_{H2O} = 0.15 bar) and syngas ($S_{0\%}$) flows at 800 ºC. (a) V-I curves. (b) Impedance curves at η_{tot} = 300 mV.

The impedance plots (Figure 4.4b) show that R_{ohm} and R_{pol} are nearly identical for the two fuels, as are the shape of the curves. This reinforces the notion that H_2 was dominating the electrochemistry with the syngas. If the CO was not reformed but instead electrochemically oxidized, the shape of the two impedance curves would be different. This is because the oxidation kinetics of CO are slower than that of H_2 (see *Section 1.3.3*) and would therefore respond differently to certain voltage frequencies.

As shown in Figure 4.5 the cell performance was consistent for all syngas conversions at 800 ºC. There was a negligible increase in performance when switching from flow $S_{0\%}$ to $S_{25\%}$ (both flows had maximum power densities of 0.26 W/cm^2) and a slight decrease in performance for the $S_{50\%}$ flow (0.24 W/cm^2). This shows that the cell experienced only minor drops in performance when operating under reduced fuel and increased product conditions, which would imply relatively even performance down the channel for a planar SOFC up to 50% syngas conversion.

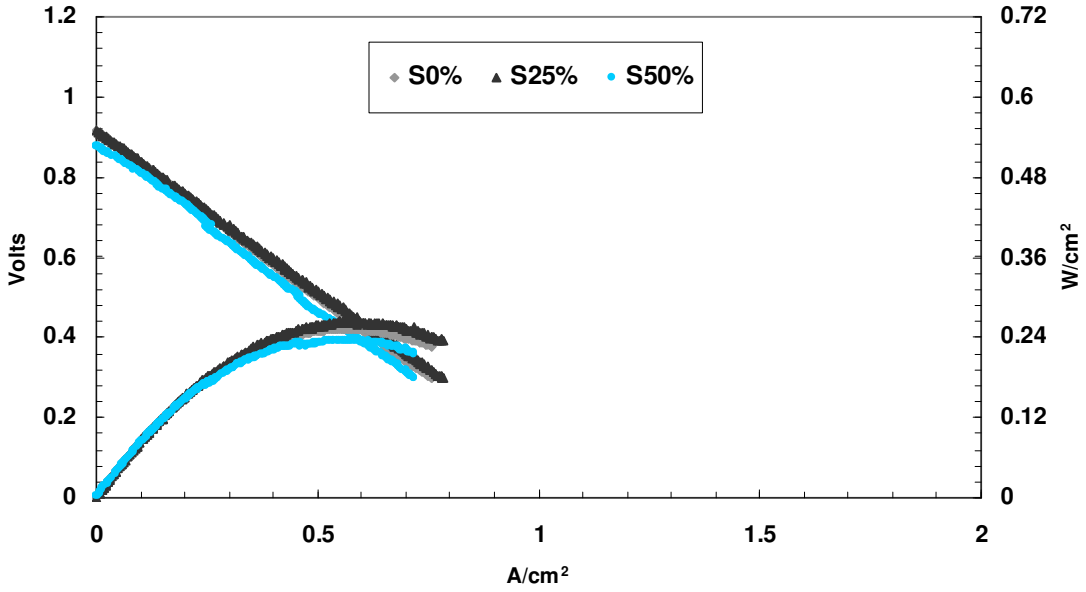

Figure 4.5 *Cell 1* V-I curves for a range of syngas compositions at 800 ºC.

Performance on syngas flows was also evaluated at temperatures of 750 and 700 ºC. As seen in Figure 4.6 for the $S_{0\%}$ flow, the performance decreased with temperature. The maximum power densities were 0.26 W/cm^2, 0.19 W/cm^2, and 0.12 W/cm^2 at 800, 750, and 700 ºC respectively. This trend was to be expected given that all three overpotentials increase with decreasing temperature. Ohmic resistances increase because YSZ O^{2-} ion conductivity drops strongly with temperature, activation overpotentials increase because the electrochemical reaction rates slow down, and concentration overpotentials increase because gases diffuse more slowly and cannot penetrate the porous electrodes as quickly.

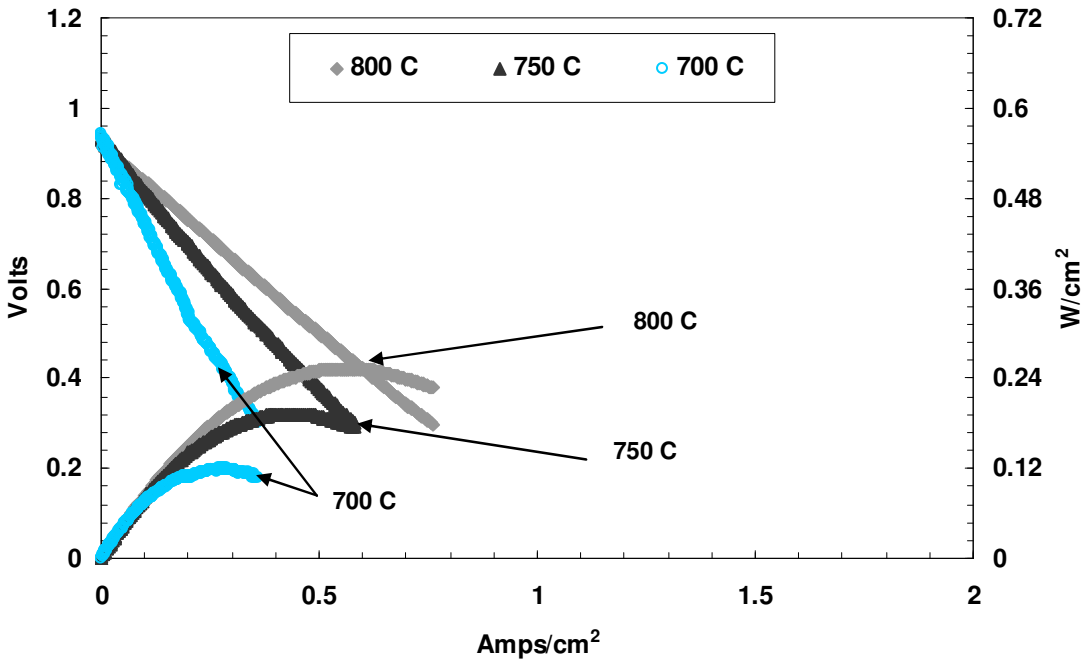

Figure 4.6 *Cell 1* performance at 800, 750, and 700 ºC for syngas mixture $S_{0\%}$.

4.3 Fitting and Determination of the Cathode Overpotentials

Since the objective of this study involves evaluation of SOFC anodes, it is critical to isolate the anode contributions to both η_{tot} and R_{pol}. Ideally, the anode overpotentials can be broken into their two principal components $\eta_{conc,a}$ and $\eta_{act,a}$. There is a small contribution to η_{ohm} from the anode due to the diffusion of O^{2-} ions into the electrolyte phase in the functional layer, but as discussed in the previous section, this contribution to η_{ohm} can be determined by measuring the changes in R_{ohm} with changes in current density.

For syngas and humidified H_2 fuel streams operating with thick anode support layers, the dominant overpotential for the anode is $\eta_{conc,a}$ [42]. To isolate these anode

overpotentials and impedance, the cathode contributions to η_{tot} and the ohmic overpotential η_{ohm} must be identified. The electrolyte and other ohmic contributions are readily identified by getting R_{ohm} from the high-frequency impedance measurements. The cathode contributions can be difficult to isolate.

To assist in isolating the cathode contributions, a detailed through-the-MEA model developed my Decaluwe et al. [42] has been employed to fit the measured performance curves to the model predictions. The model generates a V-I curve based on the values of several inputted parameters such as porosity, tortuosity, active three phase boundary length, and many others. The model was designed to simulate the performance of an MEA with a Ni/YSZ support layer, a Ni/YSZ functional layer, a YSZ electrolyte, and an LSM/YSZ cathode with an optional secondary LSM cathode layer. This composite structure makes it particularly relevant for fitting the Ni/YSZ data accumulated in this study. A table displaying the relevant input parameters utilized by the model are shown below. Parameters that were adjusted in this study to produce the best fit are highlighted.

Table 4.1 Parameters used in the model to calculate V-I curves. Parameters adjusted in this study to give the best fit are highlighted and displayed without a specific value.

	Anode	**Cathode**
TPB Length (m^{-2})	3×10^{13}	-
Average Pore Radius (μm)	0.5	0.5
Average Particle Diameter (μm)	2.5	2.5
Utilization Thickness (μm)	5	5
Support Layer Thickness (μm)	955	50
Support Layer Porosity	-	0.26
Support Layer Tortuosity	-	2.9
Functional Layer Thickness (μm)	25	30
Functional Layer Porosity	0.23	0.26
Functional Layer Tortuosity	4.5	4.5
Catalyst Fraction of Solid Phase	0.55	0.47

Electrode Site Density (mol/cm^2)	1.66 x 10^9	1.66 x 10^9
Electrolyte Site Density (mol/cm^2)	1 x 10^9	1 x 10^9
Electrolyte Surface Area (mol^{-1})	1 x 10^7	1 x 10^7
Double Layer Capacitance (F/m^3)	0.003	0.2
Sherwood Number	3	3
Electrode Surface Area (m^{-1})	1 x 10^7	-

To isolate the cathode, P_{H2O} = 0.03 bar flows, which have the smallest anode overpotentials and well understood Ni/YSZ-H_2 oxidation chemistry [42], were chosen for fitting with the model. Four model parameters, which are known to be important and not readily measured, were varied in an effort to fit the 3% humidified hydrogen data taken at 800 ºC. These parameters were:

- the anode support layer tortuosity, τ_a
- the anode support layer porosity, ϕ_a
- the cathode TPB length per unit volume of functional layer, $l_{TPB,c}$
- the cathode catalyst surface area per unit volume of functional layer, $a_{cat,c}$

The two anode parameters were selected because they affect $\eta_{conc,a}$, which tends to be much more significant than the anode activation overpotential. The cathode parameters were selected because they affect the activation overpotential which tends to be much more significant than the concentration overpotential. As will shortly be discussed, these assumptions were validated by the fits.

The model was adjusted in the way it calculated η_{ohm}. Initial attempts at fitting using a constant ohmic overpotential consistently under predicted the voltage losses in the mid-to-high current density regime (>0.4A/cm^2). As the impedance curves suggest R_{ohm} increases with current density, this under prediction was not

surprising. In this regard R_{ohm} was set to increase linearly with current density. The linear expression was determined from the high frequency intercepts of the impedance curves at η_{ohm} = 100 and 300 mV.

To fit the overpotentials properly, it was necessary to account for the differences between the theoretical and measured open-circuit voltages. It was assumed that gas diffusion through pinholes in the electrolyte led to the decrease in voltage. As the cathode side flow was always greater than the anode side flow, it was assumed that gas flowed from the cathode to the anode. It was also assumed that O_2 flowing to the anode would react in the functional layer with available H_2 and decrease the local P_{H2} while increasing the local P_{H2O}. As leakage through the electrolyte resulted in reduced reactant partial pressures, the difference between the measured and theoretical OCVs was treated as a concentration overpotential.

A series of fits were first run without accounting for gas leaks. The closest fit was isolated and the current density for which the cathode and anode concentration overpotentials combined to give the difference between the measured and theoretical OCVs (0.133 V) determined. From this initial current, termed the leakage current, the effective diffusion coefficient of oxygen through the electrolyte divided by the electrolyte thickness ($D_{eff,k}/\delta_{el}$) was found via Equation 4.1, assuming Knudsen diffusion. Here $P_{O2,el}$ is the oxygen partial pressure at the cathode/electrolyte interface at open circuit conditions. It was calculated by the model.

$$\frac{D_{eff,k}}{\delta_{el}} = \frac{i_{leak}}{4F}\left(\frac{RT}{P_{O_2,el}}\right) \qquad \text{Eq. 4.1}$$

Once the diffusion coefficient was known, the molar flux of oxygen to the anode was calculated via Equation 4.2.

$$\dot{n}_{O_2} = \frac{D_{eff,k}}{\delta_{el}}\left(\frac{P_{O_2}}{RT}\right) \qquad \text{Eq. 4.2}$$

The molar flux was used to adjust the partial pressures on the anode and cathode sides. The dependence of $\dot{n}_{O_2}$ on P_{O2} results in the leakage current correction depending on current density i, with $\dot{n}_{O_2}$ being largest at low currents (i.e., high P_{O2}) and smallest at high currents (i.e., low P_{O2}).

The final fit along with the experimental data are shown in Figure 4.7. The values of the fitted parameters are highlighted in Table 4.2.

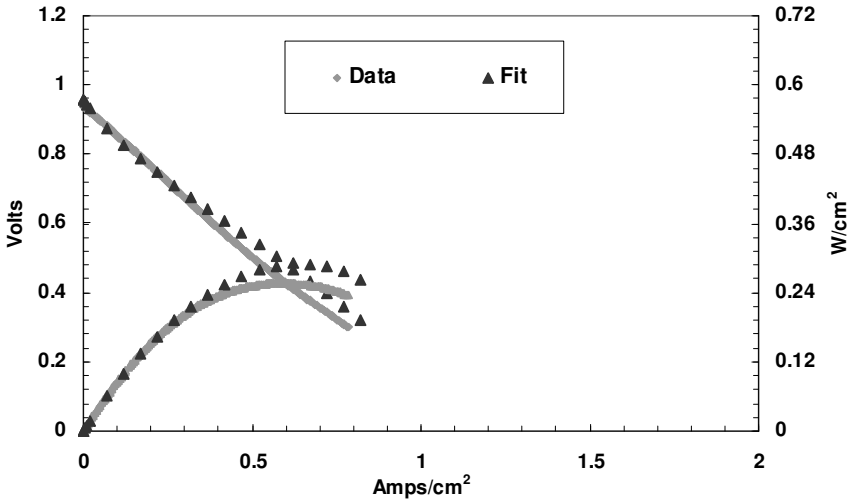

Figure 4.7 Measured and fitted values for Cell 1 operating at 800 °C for $P_{H2} = 0.485$ *bar and* $P_{H2O} = 0.03$ *bar.*

Table 4.2 Values of the fitting parameters for *Cell 1*

τ_a	ϕ_a (%)	$l_{TPB,c}$ (m/m^3)	$a_{cat,c}$ (m^2/m^3)
4.5	55	4.00E+12	1.00E+07

Although the fit captures the basic form of the data there are areas of clear deviation. At current densities lower than approximately 0.3 A/cm^2 the model slightly over-predicts the overpotentials while at current densities greater than 0.3 A/cm^2 the model under-predicts the overpotentials. As far as the under-predicted values at low current densities are concerned, it can be seen in Figure 4.8a that the cathode overpotential is most significant in the low current density range and is therefore most likely to be over-predicted. Since $\eta_{act,c}$ essentially accounts for the entire cathode overpotential (see Figure 4.8b), it is the likely value over predicted at the low *i*. For the humidified H_2 anode flows with the low P_{H2O} = 0.03 bar, $\eta_{conc,a}$ is very small at low current densities and does not contribute significantly to η_{tot}.

At current densities greater than 0.3 A/cm^2 the cathode overpotential begins to flatten out while η_{ohm} and $\eta_{conc,a}$ continue to increase. It is likely then that one of these is under-predicted by the model. As the anode contribution traditionally becomes more significant at higher current densities, particularly the concentration overpotential (see Figure 4.8b), it could be assumed that the anode concentration overpotential was under-predicted.

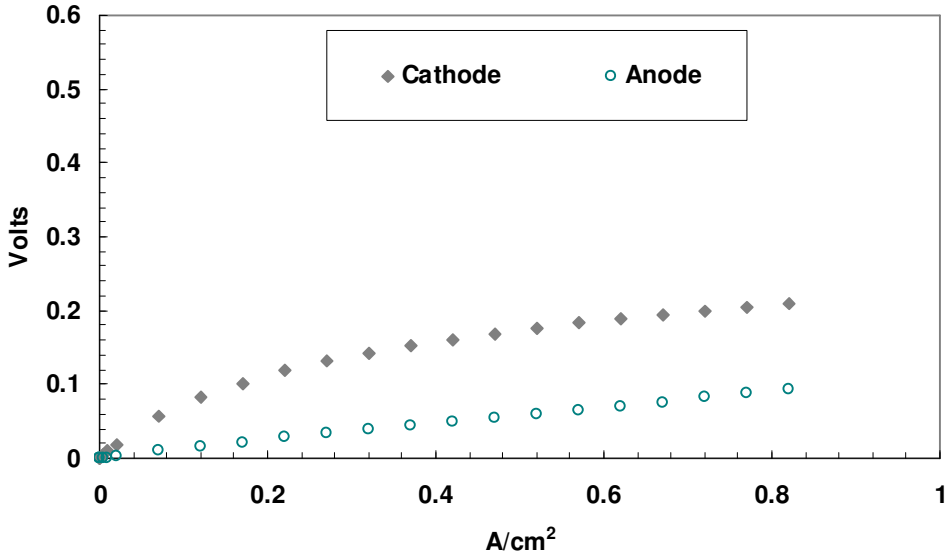

(a)

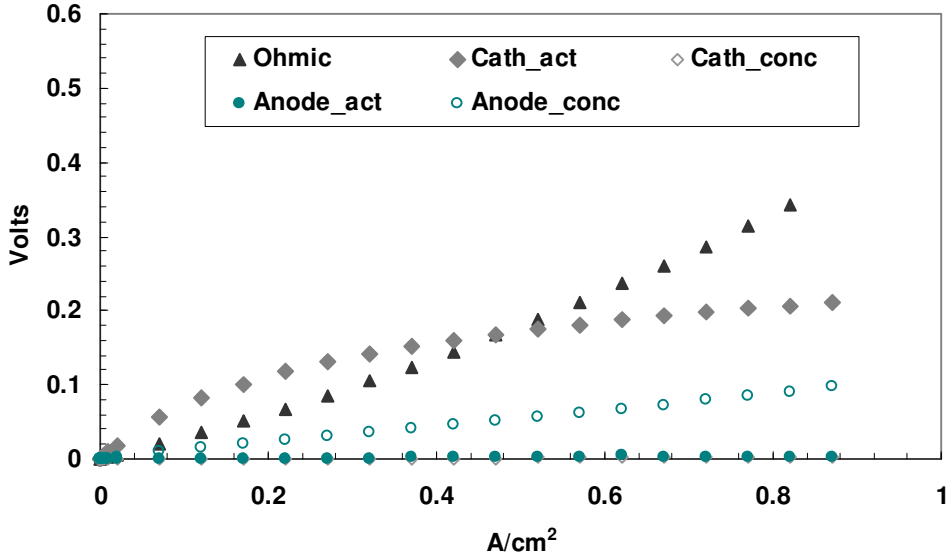

(b)

Figure 4.8 Model predicted overpotentials using the parameters provided in *Table 1* for P_{H2} = 0.485 bar and P_{H2O} = 0.03 bar. (a) Overpotentials by electrode. (b) Overpotentials by component i.e. ohmic, activation, concentration.

Fitting the data ultimately allowed the experimental anode overpotential to be isolated. The experimental anode overpotential was found by adding the fitted

cathode and calculated ohmic overpotentials to the experimental data. This is different from the fitted anode overpotential shown in Figures 4.8a in that the fitted overpotential is found by adding the cathode and ohmic overpotentials to the fit, not the data. The experimental overpotential is more useful as the anodes for cells with similar electrolytes and cathodes can be compared by using just one fit and adjusting the respective V-I curves by the determined electrolyte and cathode overpotentials.

The experimental and fitted anode overpotentials are shown in Figure 4.9. Note that the experimental overpotential dips into the negatives at current densities less than 0.3 A/cm^2 before becoming more aligned with the fitted value at higher densities. The existence of negative overpotentials is caused by the model over predicting the cathode overpotential for current densities less than 0.3 A/cm^2. When the artificially high cathode overpotential is added to the experimental data it results in a voltage higher than the OCV and therefore a negative anode overpotential.

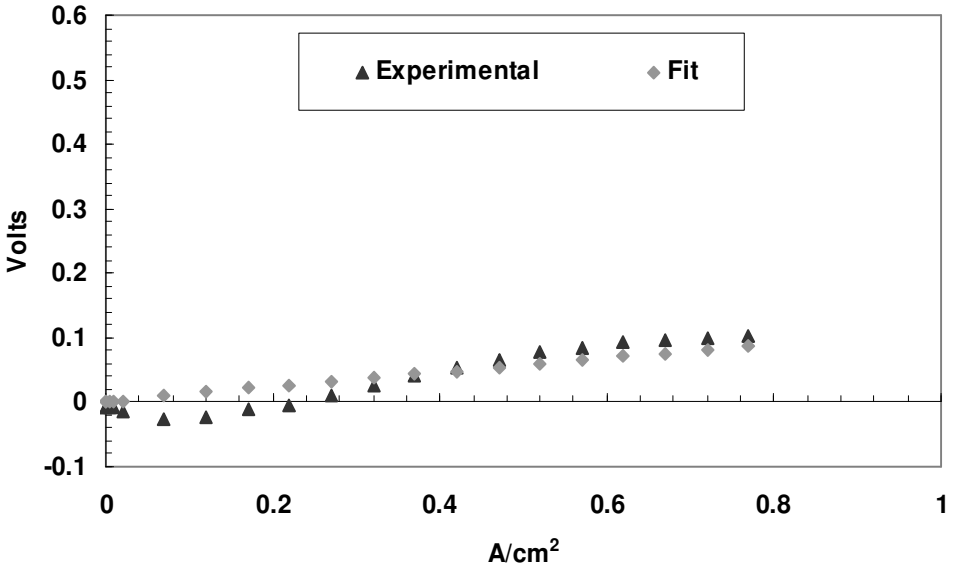

Figure 4.9 Isolated anode overpotentials for P_{H2} = 0.485 bar and P_{H2O} = 0.03 bar at 800 °C

Chapter 5: Ni/CeO_2/YSZ Anode Performance

This chapter explores the affect on anode performance of adding CeO_2 to a Ni/YSZ composite anode. Three different architectures were explored by utilizing different approaches of CeO_2 addition. The first contained CeO_2 in the support layer that was introduced by the co-firing method. The second contained CeO_2 in the anode support and functional layers that was also introduced using the co-firing method. The third introduced CeO_2 into the cell using an impregnation method. The anode performance for the three Ni/CeO_2/YSZ cells is compared to the baseline Ni/YSZ cell as well as to each other.

5.1 CeO_2 in the Support Layer

Cell 2 was fabricated with a support layer containing Ni, CeO_2, and YSZ and a functional layer containing only Ni and YSZ. Other relevant cell features are documented in Table 2.2. Although *Cell 2* was supposed to contain only nickel and YSZ in the functional layer, it was necessary to confirm the absence of CeO_2 in this layer. Energy-dispersive X-ray spectroscopy (EDS) was used for this purpose by performing an elemental line scan across the cell components. Cerium was selected for detection as a means of identifying the presence of ceria in the functional layer. Additionally, lanthanum was selected to probe the cathode micro-architecture.

As EDS only identifies elements and not molecules, the presence of cerium in a particular cell layer did not guarantee the presence of ceria. The absence of cerium, however, did guarantee the absence of ceria. The results of the scan are shown in Figure 5.1. They confirm the existence of cerium in the support layer, but not the functional layer. This validates the co-firing method as a means of constructing well-defined cell layers with different elemental compositions. The line-scan also shows a stark difference in lanthanum concentrations in the cathode. The current collecting layer contained only LSM and was not diluted with YSZ like the functional layer, which explains the difference in concentrations and confirms the cathode bi-layer structure was successfully fabricated.

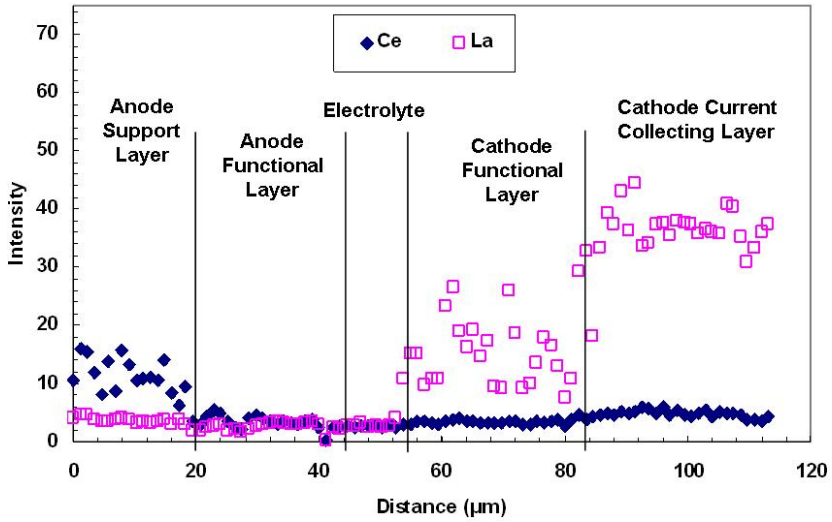

Figure 5.1 EDS line-scan across the five layers of *Cell 2*.

5.1.1 Hydrogen Testing

V-I curves for *Cell 2* operating on H_2 at 800 °C and P_{H2O} = 0.03 bar are shown in Figure 5.2 (Refer to *Table 3.1* for H_2 partial pressure information). Also included are the corresponding curves for *Cell 1*. *Cell 2* clearly out performs *Cell 1* with a maximum power density of 0.59 W/cm^2 compared to 0.26 W/cm^2. Both curves are relatively linear in shape with *Cell 2* having a shallower slope, indicating a smaller R_{tot}.

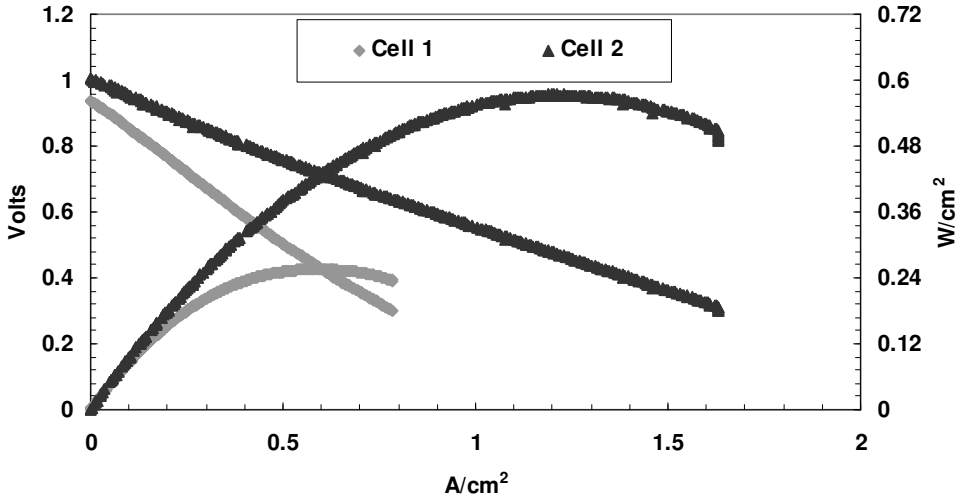

Figure 5.2 *V*-I curves for *Cells 1* and *2* operating at 800 ºC for P_{H2} = 0.485 bar and P_{H2O} = 0.03 bar.

The corresponding impedance curves at η_{tot} = 300mV are shown in Figure 5.3. R_{ohm} has been subtracted out in an effort to eliminate the electrolyte thickness difference between the cells. R_{pol} is equal to 0.60 Ω•cm^2 for *Cell 1* and is between 0.18 and 0.20 Ω•cm^2 for *Cell 2*. Because *Cell 2* did not contain CeO_2 in the functional layer, differences in electrochemical activity should be minimal between the cells. Additionally, as H_2 was the only fuel, CeO_2 in the support layer should have provided no catalytic or reforming advantage over a pure nickel cell. In this regard it was expected that R_{pol} would have been more similar for the H_2 flows.

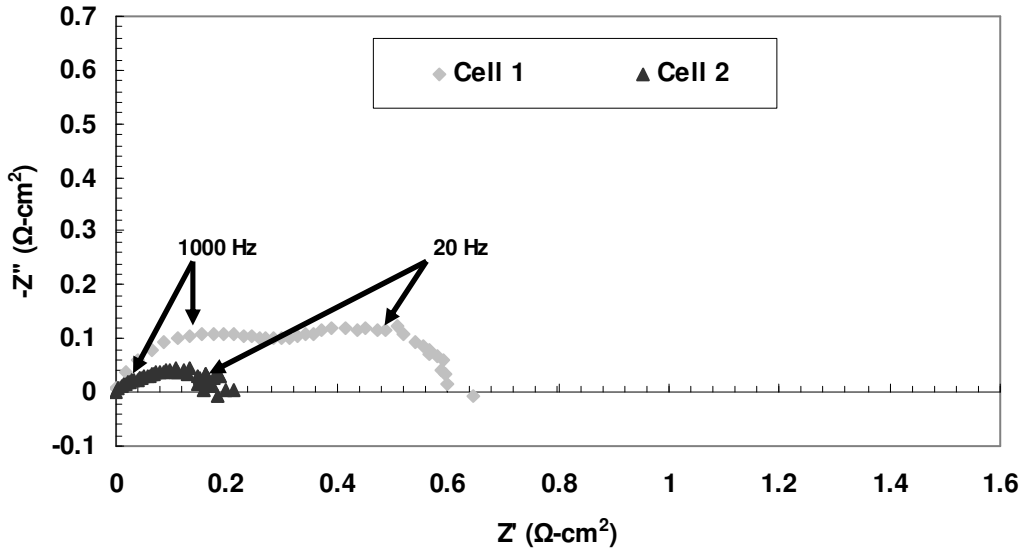

Figure 5.3 R_{pol} for *Cell 1* and *2* at 800 ºC and η_{tot} = 300mV. The flow had partial pressures of P_{H2} = 0.485 bar and P_{H2O} = 0.03 bar.

To reconcile the difference in performance, the data for *Cell 2* was fit using the model described in *Chapter 4*. The V-I curve for the P_{H2O} = 0.03 bar case was chosen for the fit. Although the model does not incorporate CeO_2 chemistry, it was assumed this did not affect the fit for *Cell 2*. This assumption was deemed valid because the anode flow only contained H_2 and because in *Cell 2* CeO_2 was not present in the functional layer and therefore could not contribute to the electrochemical activity of the cell.

The experimental curve, the fitted curve, and the fitted overpotentials are shown in Figure 5.4. The fit captures the shape and magnitude of the curve much more accurately than the fit for *Cell 1*. The values of the fitted parameters for *Cell 1* and *Cell 2* are given in Table 5.1.

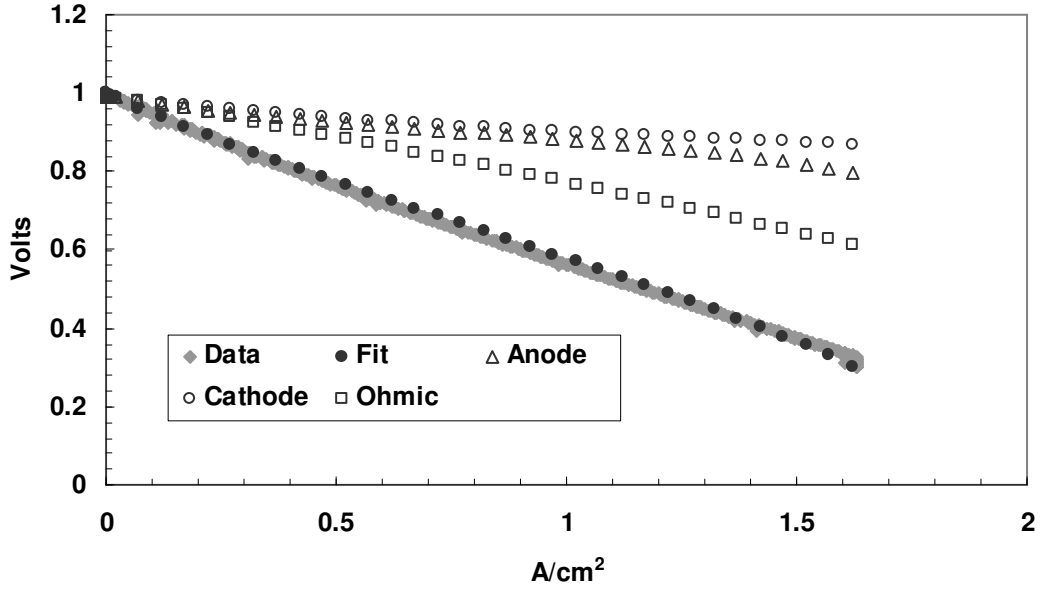

Figure 5.4 Experimental data and the corresponding fit at 800 °C, P_{H2} = 0.485 bar, and P_{H2O} = 0.03 bar (solid symbols). The fit is also separated into its anode, cathode, and ohmic components (open symbols).

Table 5.1 Values of fitted variables for *Cells 1* and *2*

	Cell 1	**Cell 2**
τ_a	4.5	3.8
ϕ_a (%)	0.55	0.5
$l_{TPB,c}$ (m/m^2 electrolyte)	4.00 x 10^{12}	3.00 x 10^{13}
$a_{cat,c}$ (m^2/m^2 electrolyte)	1.00 x 10^{7}	1.00 x 10^{7}

The values from the model seem to indicate the anode and cathode performed better for *Cell 2* than *Cell 1*. The anode tortuosity was 15.5% lower for *Cell 2* and the cathode TPB length was almost an order of magnitude larger for *Cell 2*. The difference in anode tortuosity did not result in a significant difference in anode overpotentials, however, as can be seen in Figure 5.5a. The difference between cathode TPB lengths, on the other hand, resulted in more significant overpotential differences. As can be seen in Figure 5.5b, η_c for *Cell 1* is consistently two to three

times larger than η_c for *Cell 2*. These fits imply that although the anode tortuosities were different between cells, differing cathodes were the primary reason for the performance difference.

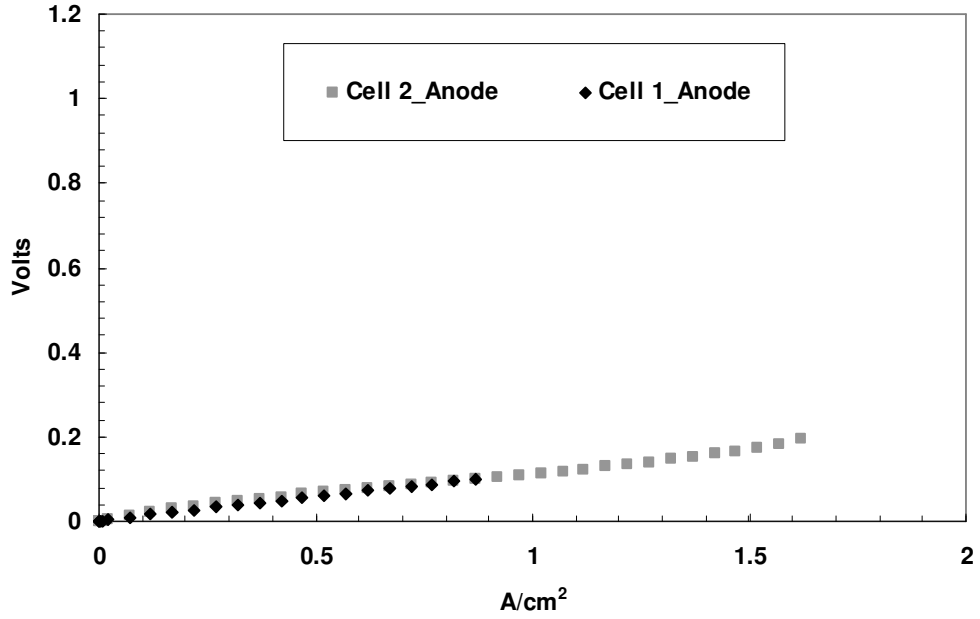

(a)

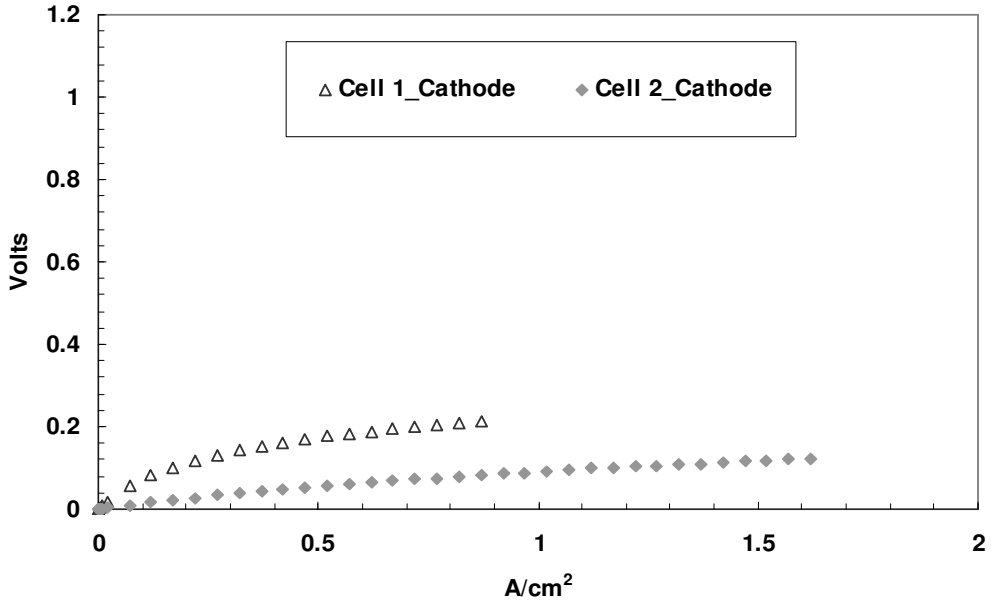

(b)

Figure 5.5 Model predicted electrode overpotentials for *Cells 1* and *2* with P_{H2} = 0.485 and P_{H2O} = 0.03 (a) Anode overpotentials. (b) Cathode Overpotentials.

It is not clear why the cathodes performed so differently. *Cell 2* utilized a bi-layer cathode, but it is difficult to believe this alone created the dramatic difference in performance. As *Cell 2* was tested two months prior to *Cell 1*, another explanation is that the properties of the purchased LSM/YSZ-composite cathode paste changed between tests. Although the manufacturer of the paste did not supply a recommended shelf life time, it is possible that the paste deteriorated between tests.

5.1.2 Syngas Testing

Results of the syngas testing at 800 ºC are shown in Figure 5.6. The maximum power densities on $S_{0\%}$, $S_{25\%}$, and $S_{50\%}$ flows were 0.55 W/cm^2, 0.53

W/cm^2, and 0.46 W/cm^2 respectively. As a reference the maximum power density obtained with an H_2 flow was 0.59 W/cm^2. There was only a slight drop in performance in switching from H_2 to syngas even for the condition of 50% syngas conversion ($S_{50\%}$). The lower performance with increased syngas conversion was probably caused by a large $\eta_{conc,a}$ resulting from the high inlet P_{H2O} = 0.405.

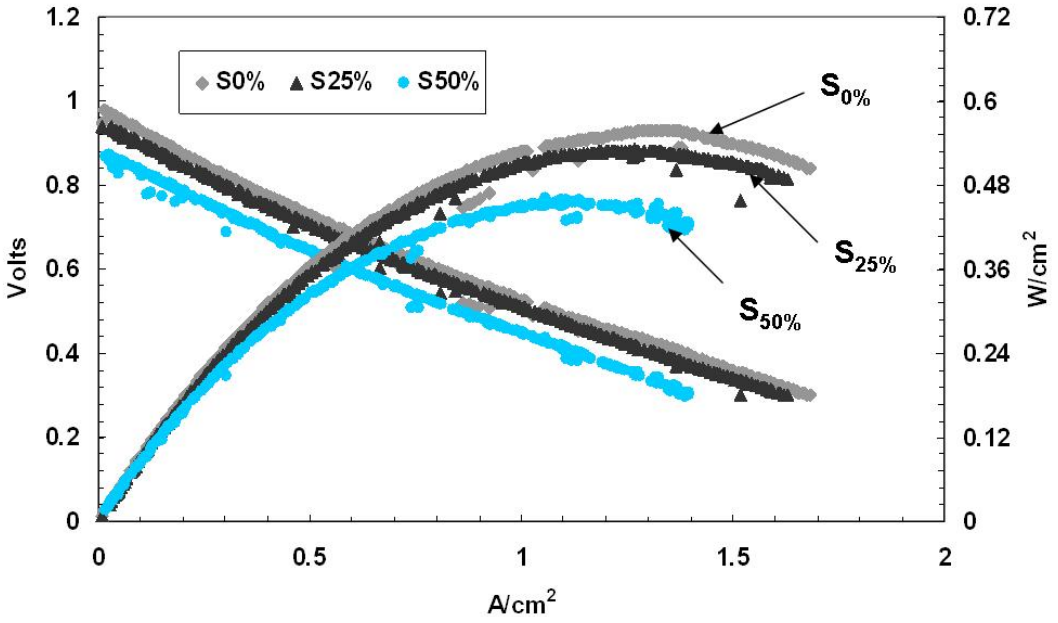

Figure 5.6 *Cell 2* operation on various syngas compositions at 800 ºC.

5.2 CeO_2 in the Support and Functional Layers

5.2.1 Hydrogen Testing

Cell 3 contained CeO_2 in both the support and functional layers and was tested to determine if CeO_2 could enhance anode performance after being heated to 1400 ºC. As *Cell 3* utilized the same cathode and electrolyte as *Cell 1*, differences in performance can be directly attributed to the anode. The performance for both cells at 800 °C and P_{H2O} = 0.03 bar is shown in Figure 5.7.

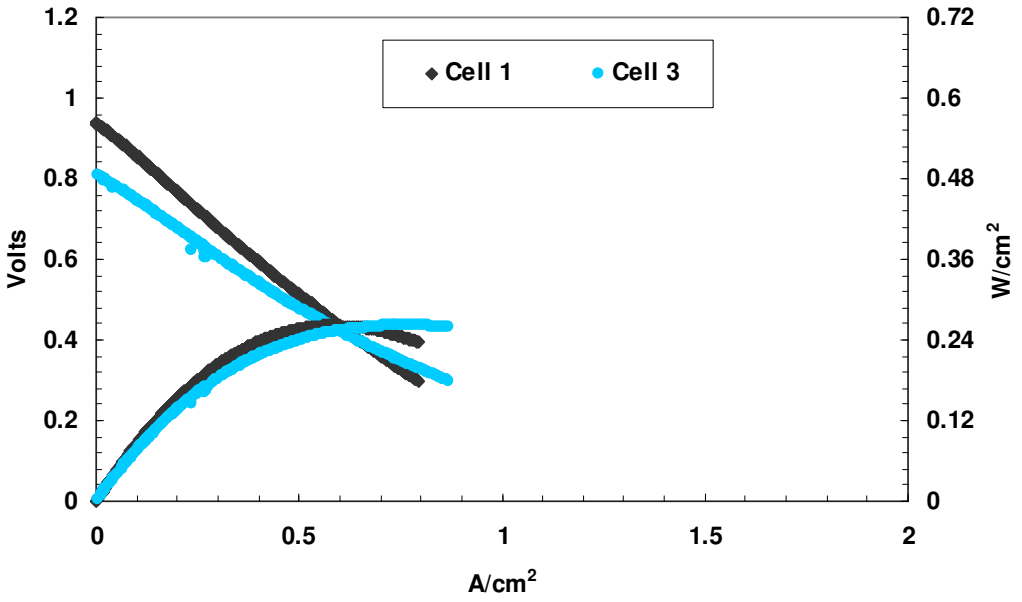

Figure 5.7 *Cell 1* and *3* V-I curves at 800 ºC, P_{H2} = 0.485 bar, and P_{H2O} = 0.03 bar.

The OCV for *Cell 3* was abnormally low at 0.82 V. Significant leaks through the electrolyte were almost certain given the relatively porous nature of the electrolyte (See Figure 5.8). Poor sealing could have been a contributor as well, but the seals appeared in good order upon inspection after cool down.

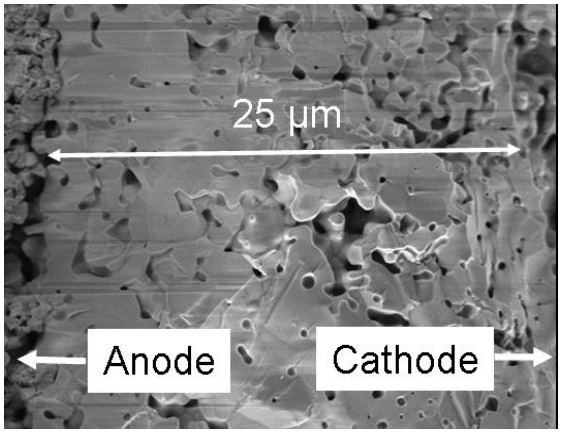

Figure 5.8 SEM of *Cell 3* showing numerous pores in the electrolyte

Another explanation is that CeO_2 migrated into the electrolyte. As CeO_2 is electronically conductive its presence in the electrolyte would lead to an electrical short and a reduced OCV. EDS analysis, however, indicated that no cerium was in the electrolyte (Figure 5.9). The low OCV can therefore not be attributed to CeO_2 in the electrolyte and was probably due to gas leaks through the electrolyte and the perimeter seal.

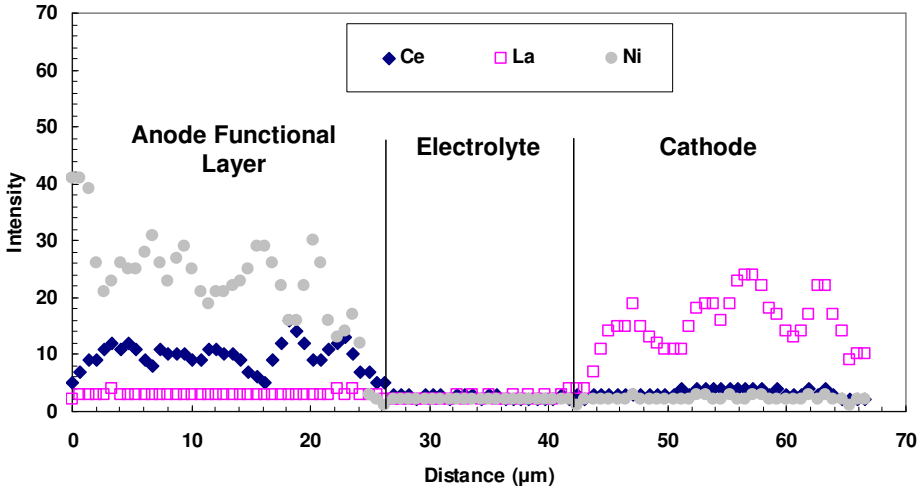

Figure 5.9 EDS line-scan showing the presence of CeO_2 in the functional layer.

The model developed by Decaluwe et al. [42] did not incorporate CeO_2 into its electrochemical calculations and was therefore not used to fit the *Cell 3* data. As the cathodes of *Cells 1* and *3* were fabricated in the same manner and contained the same microstructure, however, it was assumed that $\eta_{c,3}$ and $\eta_{c,1}$ were equal. R_{ohm} was calculated based on its value for η_{tot} = 100 mV (See Figure 5.10) and assuming it varied linearly with current at the same rate as R_{ohm} for *Cell 2*, which had a similar electrolyte thickness. The fitted $\eta_{c,3}$ and calculated $\eta_{ohm,3}$ were subtracted from $\eta_{tot,3}$ to isolate $\eta_{a,3}$.

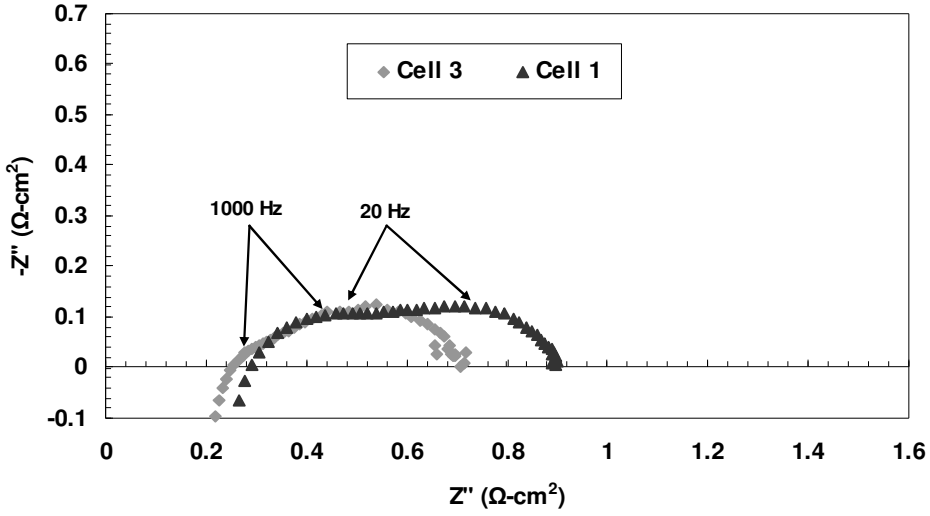

Figure 5.10 Impedance plot of *Cell 3* at 800 °C for P_{H2} = 0.485 bar, P_{H2O} = 0.03 bar, and η_{tot}= 100 mV. Characteristic frequencies of the two arcs are marked.

η_a for *Cells 1*and *3* are plotted in Figure 5.11. $\eta_{a,3}$ is consistently lower than $\eta_{a,1}$ indicating that CeO_2 in the functional and support layers appeared to improve the anode performance.

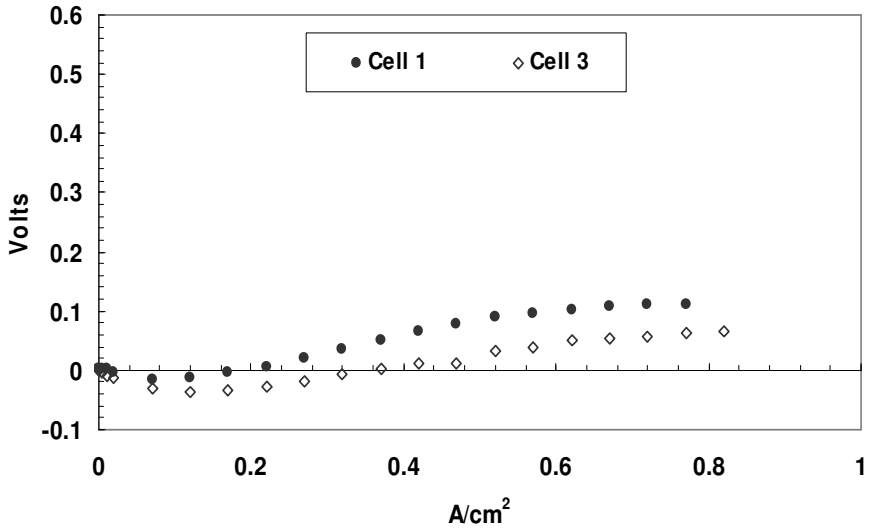

Figure 5.11 $\eta_{tot,a}$ for *Cells 1* and *3* as determined by subtracting fitted values for $\eta_{tot,c}$ and calculated values for η_{ohm} from experimental values of η_{tot}.

The impedance curves in Figure 5.10 also indicate that *Cell 3* appears to have a reduced high frequency arc compared to *Cell 1*. Again as the only difference between cells was the anode, this arc reduction must be due to an improved anode architecture. This is reinforced by looking at the Bode plots of the impedance data (Figure 5.12). Figure 5.12 shows that *Cells 1* and *3* responded similarly to frequencies between 0.1 and 20 Hz, but responded differently to frequencies greater than ~50 Hz. This means that the low frequency behavior must have been governed by cathodic processes and the high frequency behavior by anodic processes. The reduction in the high frequency impedance arc can therefore be attributed to CeO_2 in the anode.

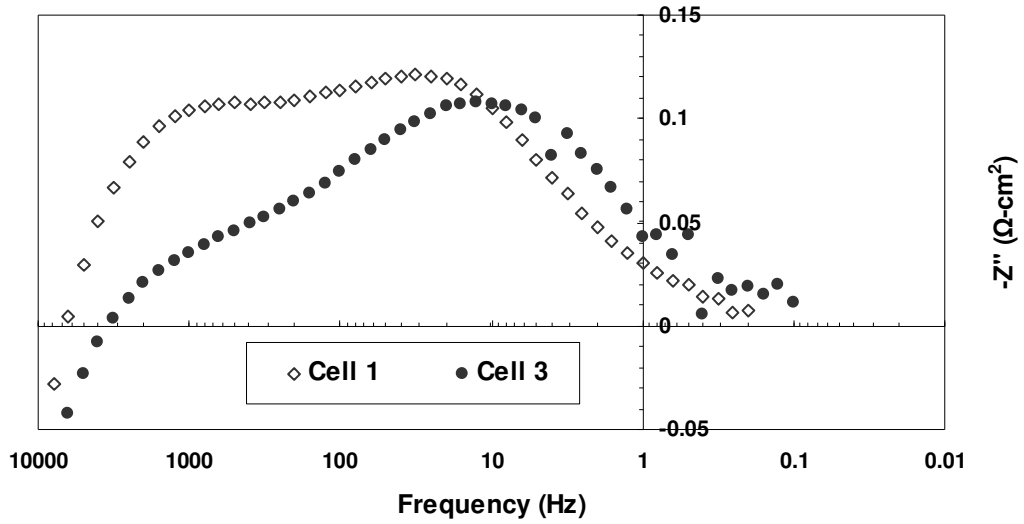

Figure 5.12 Bode plots for *Cells 1* and *3* at 800 ºC for P_{H2} = 0.485 bar, P_{H2O} = 0.03 bar and η_{tot} = 100 mV.

5.2.2 Syngas Testing

As can be seen in Figure 5.13a**,** *Cell 3* performed significantly better on syngas than on H_2. For the $S_{0\%}$ flow, the maximum power density was 0.33 W/cm^2 or 22% higher than that obtained on H_2. The impedance spectra isolated for R_{pol} (Figure 5.13b) provide insight into the reason for this performance jump. The scales in Figure 5.13b have been adjusted to allow for better inspection of the curve features. Both curves appear to have a dominant low frequency arc and an almost imperceptible high frequency arc. The high frequency anode arcs appear similar, but the low frequency arc, which was shown in Section 5.2.1 to be due to the cathode, is

clearly lower for the $S_{0\%}$ flow. Thus, changes in the cathode led to the improved performance.

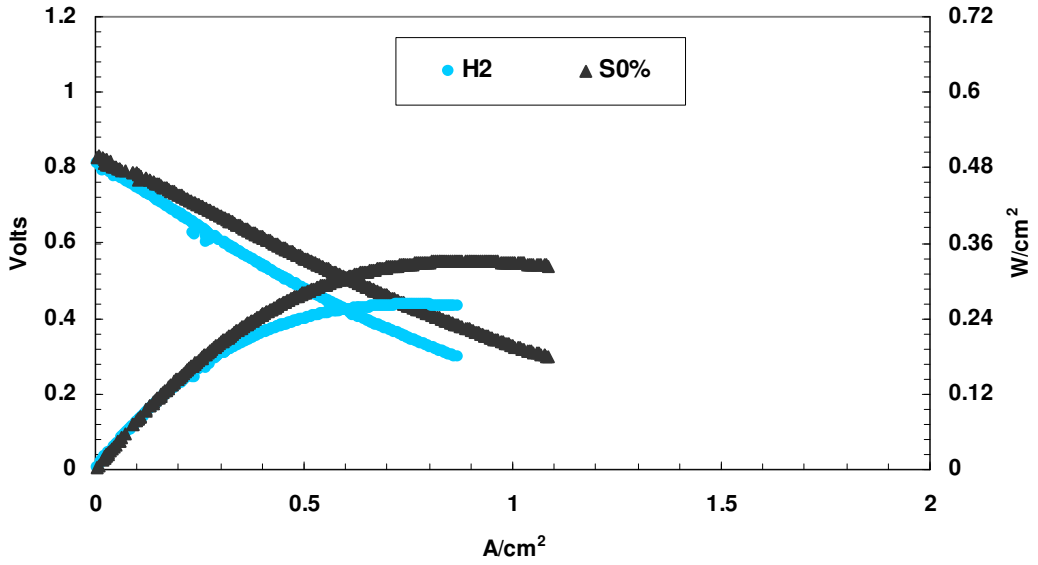

(a)

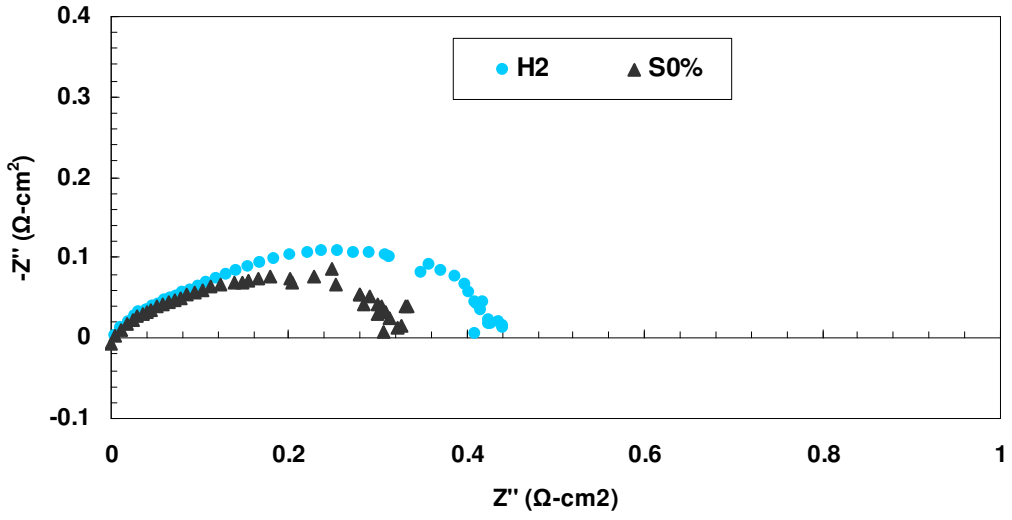

(b)

Figure 5.13 Comparison of H_2 (P_{H2} = 0.485 bar and P_{H2O} = 0.03) and syngas ($S_{0\%}$) flows at 800 °C for Cell 3. (a) V-I curves. (b) R_{pol} isolated impedance curves at η_{tot}= 100 mV. Scales adjusted to allow for easier inspection of curve features.

5.3 CeO_2 Impregnation

CeO_2 was introduced into *Cell 4* via the wet impregnation process. As the impregnation solution probed every pore and crevice of the cell, the CeO_2 distribution between anode support and functional layers was uncertain. A line-scan was performed in order to gain a better understanding of where the CeO_2 was located. As can be seen in Figure 5.14a, the CeO_2 content was relatively high in the cathode, low in the electrolyte, moderate in the anode functional layer, and low to non-existent in the anode support layer. This suggests that the CeO_2 solution passed through the electrolyte and pooled in the cathode. This was both unexpected and unintended.

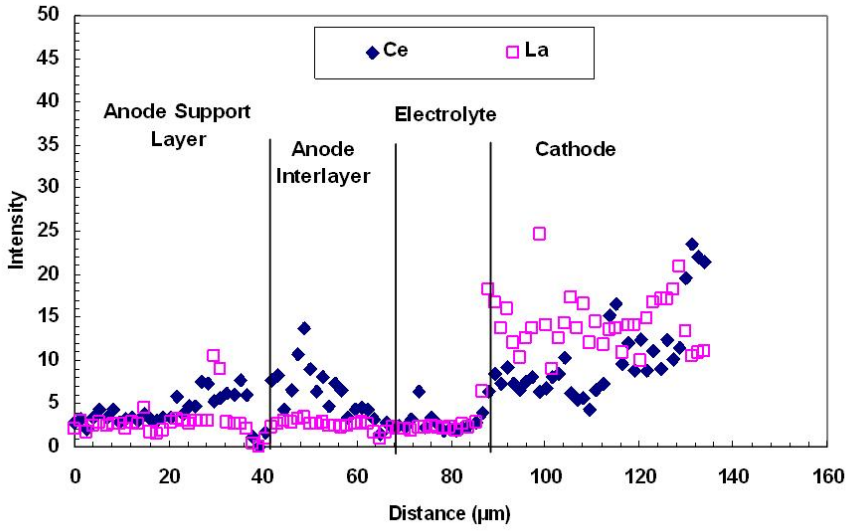

(a)

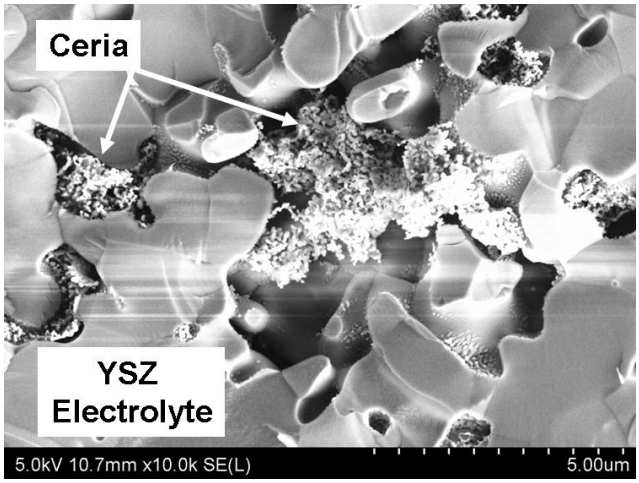

(b)

Figure 5.14 (a) Line-scan across *Cell 4* showing CeO_2 in the cathode. (b) SEM image of CeO_2 in the electrolyte of *Cell 4*.

The line-scan also suggests CeO_2 did not accumulate in the electrolyte. SEM images of the electrolyte were taken to verify this. As can be seen in Figure 5.14b CeO_2 was in fact present in the electrolyte. The CeO_2 was isolated to pores, however, and so the line-scan would not have picked it up unless specifically set to travel over a pore. Even though CeO_2 was in the electrolyte and cathode, making it more difficult to compare performance with other cells, testing was still performed. It should be noted, however, that upon completion of testing with water, the OCV spontaneously dropped and became unstable. It was ultimately determined to be too unstable to allow for accurate testing on syngas fuels.

V-I curves for *Cells 1* and *4* at 800 °C operating on H_2 and P_{H2O} = 0.03 bar are shown in Figure 5.15a. *Cell 4* had a maximum power density of 0.36 W/cm^2, compared to 0.26 W/cm^2 for *Cell 1*. Bode and impedance plots (isolated for R_{pol}) taken at η_{tot} = 300mV are also shown for the same conditions (Figure 5.15b, c).

The shape of the *Cell 4* curve in the Bode plot suggests the low frequency arc seen in the *Cell 1* curve is shifted to higher frequencies. This results in the two arcs overlapping in Figure 5.15b. As the low frequency arc is associated with the cathode, the shift in the Bode plot indicates there is a fundamental difference between the cathodes of *Cell 1* and *3*. This is to be expected given the existence of CeO_2 in the cathode of *Cell 4*.

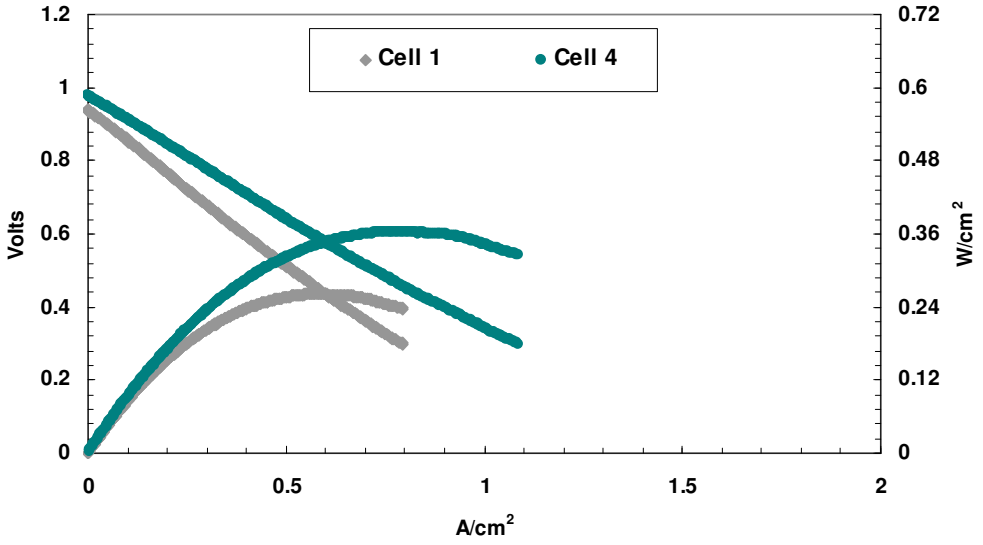

(a)

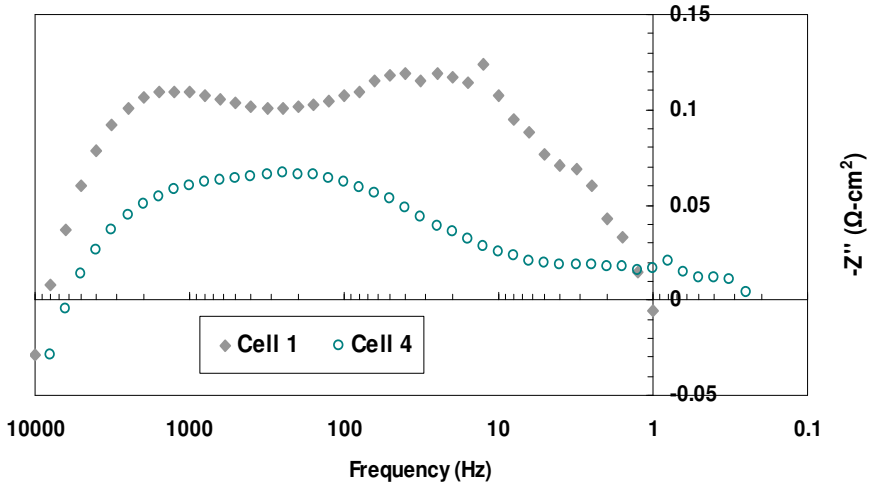

(b)

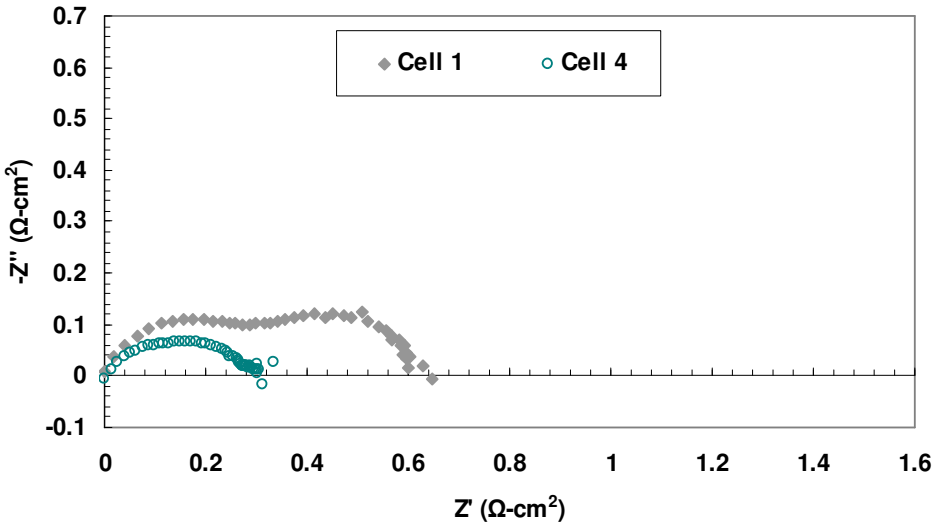

(c)

Figure 5.15 Operation on H_2 at 800 °C for *Cells 1* and *4*. (a) V-I curves (b) Bode plot at η_{tot} = 100 mV (c) Impedance spectra at η_{tot} = 100 mV

CeO_2 in the cathode appears to have improved cell performance. The impedance plots isolated for R_{pol} (Figure 5.15c) indicate *Cell 4* has half the polarization resistance of *Cell 1* (0.30 Ω·cm^2 for *Cell 4*; 0.60 Ω·cm^2 for *Cell 1*). As the anode and cathode contributions are non-zero in the *Cell 4* impedance plot, a reduction by half in R_{pol} is only possible if both the anode and cathode resistances decreased. This means that the impregnated CeO_2 not only improved the performance of the anode, but the cathode as well.

It is believed that CeO_2 improved the anode performance by generating additional TPB length. As CeO_2 was not mixed into the bulk of the anode but rather coated onto Ni/YSZ surfaces, the CeO_2 was in intimate contact with the gas. Additionally, SEM images taken of the anode show the CeO_2 formed structures on the Ni/YSZ framework with length scales on the order of tens of nanometers. As these length scales were approximately one to two orders of magnitude smaller than

that of the Ni/YSZ particles (see Figure 5.16), the CeO_2 nano-structures significantly enhanced the TPB length. As CeO_2 was found in the functional layer, additional TPB length in the electrochemically active portion of the cell would in turn improve the anode performance.

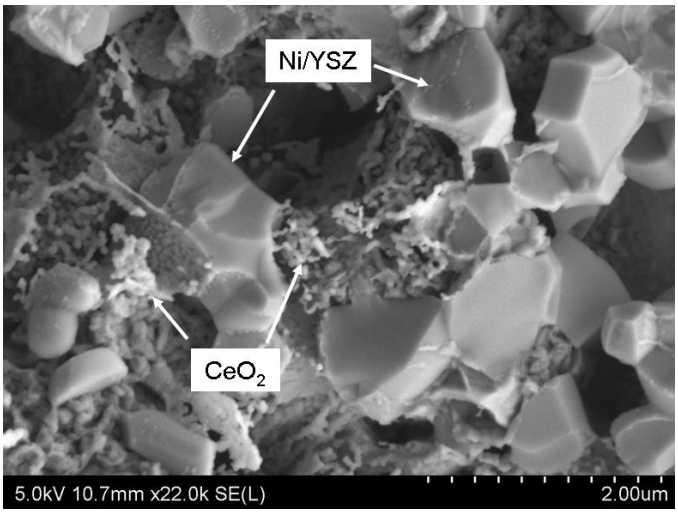

Figure 5.16 Impregnated CeO_2 nano-structures coating Ni/YSZ particles in *Cell 4*.

Similar nanostructures were present in the cathode, but it is not clear what role they played in improving performance. Although a common material in anodes, CeO_2 is not commonly used in cathodes. Doped ceria layers are sometimes placed between cathode and electrolyte layers to prevent deleterious solid state reactions between cathode catalysts and the electrolyte, but it is not clear if studies have been performed using CeO_2 directly in the cathode.

This data set was not fit using the model nor was it adjusted by values obtained for η_c and η_{ohm} from other fits. The reason for this is that CeO_2 in the cathode would compromise any attempt to adjust the data. The model does not incorporate CeO_2 chemistry in the cathode so it makes no sense to attempt a fit in that

regard. Subtracting out η_c that has been determined from a fit of *Cell 1* or *Cell 2* does not make sense either as neither of the cathodes in these cells contained CeO_2. Impedance spectra analysis was therefore the only means of isolating the anode performance.

5.4 Comparison of Cell Architectures

In the previous sections, different CeO_2 architectures were compared with a baseline Ni/YSZ cell. It was found that all three cells with CeO_2 in the anode outperformed the baseline case for both H_2 and syngas fuels (except for *Cell 4* which was not tested on syngas). The CeO_2 containing anodes are compared with each other in this section.

Figure 5.17 shows the R_{pol} isolated impedance curves at η_{tot}= *100 mV* for the three CeO_2 cells operating on H_2 with P_{H2O} = 0.03 bar. An adjusted scale is used to better highlight the curves. R_{pol} is largest for *Cell 3*, but most of this resistance is due to the cathode. The anode arc is smaller in comparison with the cathode arc and also clearly smaller than the anode arc for *Cell 4*. Although this implies the anode for *Cell 3* was better than the anode for *Cell 4*, it does not imply that the co-firing method was a better means of introducing CeO_2 than impregnation. Further tests in which CeO_2 is not present in the electrolyte and cathode need to be performed before one method can be selected as superior to the other. It is not clear upon visual inspection whether the anode arc for *Cell 2* is larger or smaller than the anode arc for *Cell 3*.

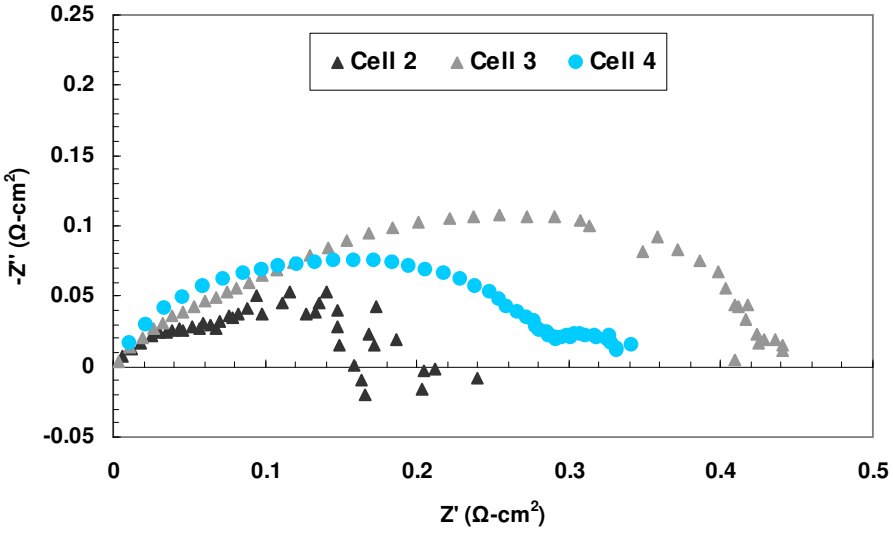

Figure 5.17 R_{pol} isolated impedance spectra for operation on H_2 at 800 °C for Cells 2, 3, and 4 at η_{tot} = 100 mV. Scales are adjusted to allow for better inspection of the curves.

V-I curves with iR_{ohm} subtracted out are shown in Figure 5.18 for *Cells 1-3* operating on the $S_{0\%}$ syngas flow (syngas tests were not performed on *Cell 4*). As with the H_2 flows, cells containing CeO_2 in the anode performed better than the baseline cell. As *Cell 2* had a different cathode and electrolyte than the baseline case, it is difficult to conclude that CeO_2 was the reason for the performance increase. *Cell 3*, however, utilized a similar cathode and electrolyte making the increase in performance likely due to CeO_2 in the anode.

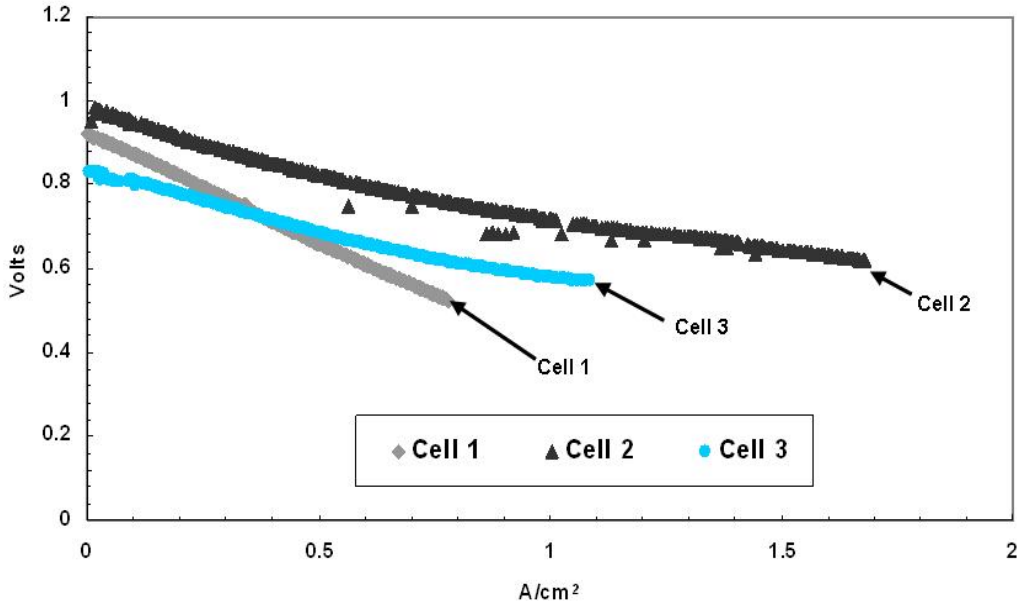

Figure 5.18 iR_{ohm} corrected V-I curves at 800 °C for operation on syngas ($S_{0\%}$).

The ohmic corrected impedance spectra for *Cells 1-3* operating on syngas at 800 °C are shown in Figure 5.19. The scales of the figure have been adjusted to allow for better inspection of the curves. Characteristic frequencies have been marked to better identify the high and low frequency arcs. Note that R_{pol} for *Cells 2* and *3* is 0.30 Ω•cm^2. This implies that the cells demonstrated similar performance at η_{tot} = 100mV. This is corroborated by the V-I curves (Figure 5.18) where the slopes of the two curves are similar in the low current regime.

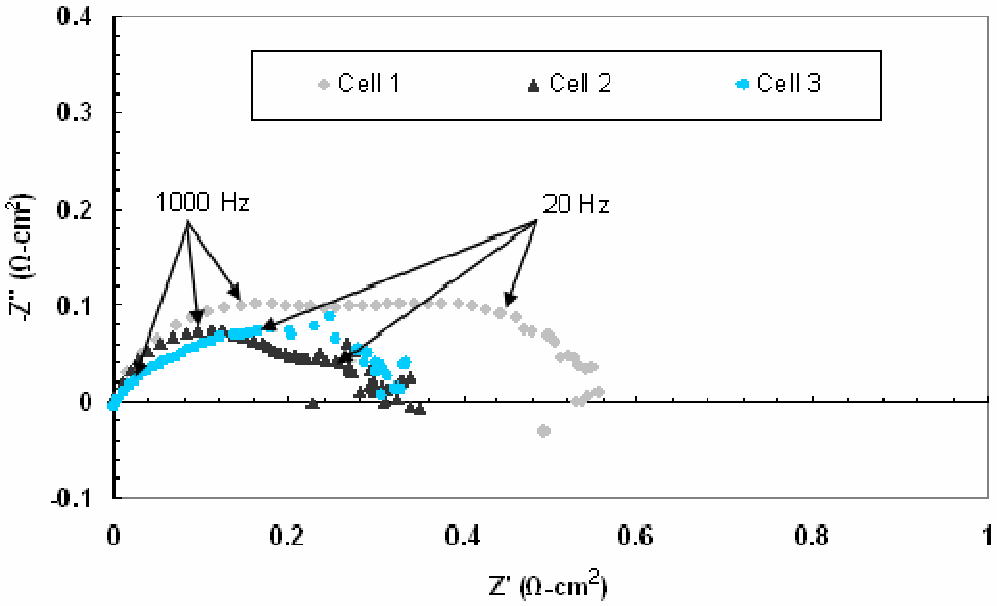

Figure 5.19 Ohmic corrected impedance plots of *Cells 1, 2,* and *3* operating on syngas ($S_{0\%}$) at 800 °C with η_{tot} = 100 mV.

Cell 2 has a major high frequency arc and a minor low frequency arc while *Cell 3* has a minor high frequency arc and a major low frequency arc. This demonstrates that *Cell 2* had the superior cathode but the inferior anode, while *Cell 3* had the superior anode but the inferior cathode. As the anode support layer was the same for *Cells 2* and *3*, the only difference between anodes was the functional layer. Given that the functional layer of *Cell 3* contained CeO_2 while the functional layer of *Cell 2* did not, the presence of CeO_2 in the functional layer led to the improved anode performance. This is despite the fact that the CeO_2 was heated above temperatures believed to lead to electrocatalytic deactivation [5].

The presence of CeO_2 within the anodes clearly led to an improvement in performance. Additional testing should explore the differences in CeO_2 introduction methods and determine if the impregnation and co-firing methods lead to similar

performance trends. Analysis of the data indicated that the anode architecture of *Cell 3* was the best architecture of the tested cells. This shows that CeO_2 in the support and functional layers can improve SOFC performance on H_2 and syngas fuels.

Chapter 6: Conclusions

Solid oxide fuel cells are a clean energy technology that can operate on H_2 as well as carbon base fuels such as carbon monoxide, methane, and butane. Reliable and lengthy operation on carbonaceous fuels, however, has proven difficult due to the propensity of SOFC anodes to catalyze the formation of carbon. Ni/YSZ anodes in particular are prone to carbon deposition. CeO_2 based anodes, on the other hand, can operate stably on fuels such as carbon monoxide and methane without forming carbon. This study looked to create a high performance CO tolerant anode by combining the traditional and well understood Ni/YSZ electrochemistry with the carbon tolerance and stability of CeO_2.

6.1 Summary of Results

Fabrication protocols were developed for anode supported solid oxide fuel cells utilizing Ni/YSZ and Ni/CeO_2/YSZ anodes. Two different methods were used to add CeO_2 to the anode. The co-firing method successfully created cell layers with distinct elemental compositions. The impregnation method, however, was not as successful. Pores in the electrolyte allowed for CeO_2 infiltration into the cathode and electrolyte. This not only reduced the CeO_2 content in the anode, but altered the performance of the cathode and may have destabilized the electrolyte.

Three SOFC MEAs with Ni/CeO_2/YSZ anodes were tested and compared with a baseline Ni/YSZ anode. A summary of the three architectures are as follows:

- Cell 2: Fabricated by co-firing CeO_2 with NiO and YSZ in the initial anode fabrication step. Contained CeO_2 in the support layer only.
- Cell 3: Fabricated by co-firing CeO_2 with NiO and YSZ in the initial anode fabrication step. Contained CeO_2 in the support and functional layer.
- Cell 4: Fabricated by impregnating CeO_2 into a highly porous Ni/YSZ anode that had already been fired at high temperatures. Contained CeO_2 in the anode, cathode, and electrolyte.

Each of these cells demonstrated a higher power density than the Ni/YSZ cell when operating on H_2. The two CeO_2-containing MEAs fabricated using the co-fired method also demonstrated higher power densities for operation on syngas. The CeO_2 MEA fabricated via the impregnation method was not tested on syngas due to a cell failure after H_2 testing. This failure was attributed to the impregnated CeO_2 penetrating into the electrolyte and compromising the MEA's structural integrity.

Data analysis and fitting were then performed to allow for comparison between cell electrodes. Comparison between cell electrodes led to the following two important conclusions:

- The presence of CeO_2 in Ni/YSZ anodes led to higher power densities and reduced polarization resistances when operating on H_2 and syngas fuel feeds, even after sintering at 1400 °C.
- CeO_2 in the functional layer led to a reduced high-frequency impedance arc, indicating that CeO_2 may enhance electrochemical activity

6.2 Recommendations for Future Work

Although several cells were successfully tested without failure, the fabrication protocol, which followed closely earlier work reported in the literature, did not always produce reliable cells that maintained their structural integrity in the experimental rig [9, 38, 39]. Cells failed due to cracked electrolyte membranes and/or poor sealing around the anode edges. There were often trade-offs between good sealing and minimizing the risk of cracking the thin electrolyte membrane. The ceramic paste sealing method sealed the cell well, but consistently led to cell cracks. A way to increase cell robustness is to increase the YSZ content in the support layer. This study utilized a NiO:YSZ weight ratio of 7:3. Decreasing this ratio to 3:2 or 1:1 would lead to a more extensive YSZ support framework. Increasing the sintering temperature may also lead to more extensive YSZ sintering and result in a stronger, more durable cell. It may also reduce the electrolyte porosity and allow for more consistent impregnation testing.

Although there were difficulties encountered in the fabrication and testing processes, this study successfully fabricated and tested several Ni/CeO2-YSZ cells. Furthermore, two of these cells (*Cells 2* and *3*) were operated stably on syngas and hydrogen fuels while outperforming the Ni/YSZ baseline cell. Testing should next be performed on hydrocarbons such as methane or butane to evaluate the stability of Ni/CeO_2/YSZ anodes on direct hydrocarbon fuel feeds. Testing on butane is the next logical step to take now that much of the fabrication and early testing groundwork have been successfully completed.

Bibliography

1. McIntosh, S. and R.J. Gorte, *Direct hydrocarbon solid oxide fuel cells.* Chemical Reviews, 2004. 104(10): p. 4845-4865.
2. Kee, R.J., et al., *Solid Oxide Fuel Cells: Operating Principles, Current Challenges, and the Role of Syngas.* Combustion Science and Technology, 2008(180): p. 1207-1244.
3. Atkinson, A., et al., *Advanced anodes for high-temperature fuel cells.* Nature Materials, 2004. 3(1): p. 17-27.
4. Costa-Nunes, O., *Comparison of the performance of Cu-CeO2-YSZ and Ni-YSZ composite SOFC anodes with H-2, CO, and syngas.* Journal Of Power Sources, 2005. 141(2): p. 241-249.
5. He, H.P., *Effect of synthesis conditions on the performance of Cu-CeO2-YSZ anodes in SOFCs.* Journal Of The Electrochemical Society, 2003. 150(11): p. A1470-A1475.
6. McIntosh, S., J.M. Vohs, and R.J. Gorte, *Impedance spectroscopy for the characterization of Cu-Ceria-YSZ anodes for SOFCs.* Journal Of The Electrochemical Society, 2003. 150(10): p. A1305-A1312.
7. Jeon, D., Jin Nam, Charn-Junk Kim, *Microstructural Optimization of Anode-Supported Solid Oxide Fuel Cells by a Comprehensive Microscale Model.* Journal of The Electrochemical Society, 2006. 153: p. A406-A417.
8. Zhao, F. and A.V. Virkar, *Dependence of polarization in anode-supported solid oxide fuel cells on various cell parameters.* Journal Of Power Sources, 2005. 141(1): p. 79-95.
9. Armstrong, T.J. and J.G. Rich, *Anode-supported solid oxide fuel cells with La0.6Sr0.4CoO3-lambda-Zr0.84Y0.16O2-delta composite cathodes fabricated by an infiltration method.* Journal Of The Electrochemical Society, 2006. 153(3): p. A515-A520.
10. deSouza, S., *Thin-film solid oxide fuel cell with high performance at low-temperature.* Solid State Ionics, 1997. 98(1-2): p. 57-61.
11. McIntosh, S., J.M. Vohs, and R.J. Gorte, *Role of hydrocarbon deposits in the enhanced performance of direct-oxidation SOFCs.* Journal Of The Electrochemical Society, 2003. 150(4): p. A470-A476.
12. Zha, S.W., *GDC-based low-temperature SOFCs powered by hydrocarbon fuels.* Journal Of The Electrochemical Society, 2004. 151(8): p. A1128-A1133.
13. Yoo, Y., *Fabrication and characterization of thin film electrolytes deposited by RF magnetron sputtering for low temperature solid oxide fuel cells.* Journal Of Power Sources, 2006. 160(1): p. 202-206.
14. Zhu, W., et al., *Ceria coated Ni as anodes for direct utilization of methane in low-temperature solid oxide fuel cells.* Journal Of Power Sources, 2006. 160(2): p. 897-902.
15. Ivers-Tiffee, E. and A.V. Virkar, *Electrode Polarisations*, in *High Temperature Solid Oxide Fuel Cells: Fundamentals, Design, and*

Applications, S.C. Singhal and K. Kendell, Editors. 2003, Elsevier Ltd.: Bodmin.
16. Ormerod, R., *Fuels and Fuel Processing*, in *High Temperature Solid Oxide Fuel Cells: Fundamentals, Design, and Applications*, S.C. Singhal and K. Kendell, Editors. 2003, Elsevier Ltd.: Bodmin.
17. Fergus, J.W., *Electrolytes for solid oxide fuel cells.* Journal Of Power Sources, 2006. 162(1): p. 30-40.
18. Ishihara, T., N. Sammes, and O. Yamamoto, *Electrolytes*, in *High Temperature Solid Oxide Fuel Cells: Fundamentals, Design, and Applications*, S.C. Singhal and K. Kendell, Editors. 2003, Elsevier Ltd.: Bodmin.
19. Yokokawa, H. and T. Horita, *Cathodes*, in *High Temperature Solid Oxide Fuel Cells: Fundamentals, Design, and Applications*, S.C. Singhal and K. Kendell, Editors. 2003, Elsevier Ltd.: Bodmin.
20. Armstrong, T.J., *Performance of solid oxide fuel cells with LSGM-LSM composite cathodes.* Journal Of The Electrochemical Society, 2002. 149(12): p. A1565-A1571.
21. Mai, A., *Ferrite-based perovskites as cathode materials for anode-supported solid oxide fuel cells Part I. Variation of composition.* Solid State Ionics, 2005. 176(15-16): p. 1341-1350.
22. Laberty, C., *High-performance solid oxide fuel cell cathodes with lanthanum-nickelate-based composites.* Electrochemical And Solid State Letters, 2007. 10(10): p. B170-B174.
23. Lin, Y.B., et al., *Direct operation of solid oxide fuel cells with methane fuel.* Solid State Ionics, 2005. 176(23-24): p. 1827-1835.
24. Suwanwarangkul, R., *Experimental and modeling study of solid oxide fuel cell operating with syngas fuel.* Journal Of Power Sources, 2006. 161(1): p. 308-322.
25. Jiang, Y., *Fuel composition and diluent effect on gas transport and performance of anode-supported SOFCs.* Journal Of The Electrochemical Society, 2003. 150(7): p. A942-A951.
26. Matsuzaki, Y., *Electrochemical oxidation of H-2 and CO in a H-2-H2O-CO-CO2 system at the interface of a Ni-YSZ cermet electrode and YSZ electrolyte.* Journal Of The Electrochemical Society, 2000. 147(5): p. 1630-1635.
27. Sasaki, K., *Current-voltage characteristics and impedance analysis of solid oxide fuel cells for mixed H-2 and CO gases.* Journal Of The Electrochemical Society, 2002. 149(3): p. A227-A233.
28. Gorte, R.J., *Anodes for direct oxidation of dry hydrocarbons in a solid-oxide fuel cell.* Advanced Materials, 2000. 12(19): p. 1465-1469.
29. Park, S., et al., *Direct oxidation of hydrocarbons in a solid oxide fuel cell I. Methane oxidation.* Journal Of The Electrochemical Society, 1999. 146(10): p. 3603-3605.
30. Zhou, Z.F., et al., *Direct oxidation of jet fuels and Pennsylvania crude oil in a solid oxide fuel cell.* Journal Of Power Sources, 2004. 133(2): p. 181-187.
31. Qiao, J.S., *Ni/YSZ and Ni-CeO2/YSZ anodes prepared by impregnation for solid oxide fuel cells.* Journal Of Power Sources, 2007. 169(2): p. 253-258.

32. Trembly, J.P., *Effects of coal syngas and H2S on the performance of solid oxide fuel cells: Single-cell tests.* Journal Of Power Sources, 2006. 158(1): p. 263-273.
33. Kurokawa, H., *Ceria nanocoating for sulfur tolerant Ni-based anodes of solid oxide fuel cells.* Electrochemical And Solid State Letters, 2007. 10(9): p. B135-B138.
34. Johnson, M.R., *A characterization of solution gas flaring in Alberta.* Journal Of The Air & Waste Management Association, 2001. 51(8): p. 1167-1177.
35. Yoon, S.P., *Improvement of anode performance by surface modification for solid oxide fuel cell running on hydrocarbon fuel.* Journal Of Power Sources, 2004. 136(1): p. 30-36.
36. Kawano, M., et al., *Steam Reforming on Ni-Samaria-Doped Ceria Cermet Anode for Practical Size Solid Oxide Fuel Cell At Intermediate Temperatures.* Journal Of Power Sources, 2008. 182(2): p. 496-502.
37. Wang, J.B., *Study of Ni-samaria-doped ceria anode for direct oxidation of methane in solid oxide fuel cells.* Journal Of Power Sources, 2003. 122(2): p. 122-131.
38. Koh, Y.H., *Design and fabrication of three-dimensional solid oxide fuel cells.* Journal Of Power Sources, 2006. 161(2): p. 1023-1029.
39. Craciun, R., *A novel method for preparing anode cermets for solid oxide fuel cells.* Journal Of The Electrochemical Society, 1999. 146(11): p. 4019-4022.
40. McEvoy, A., *Anodes*, in *High Temperature Solid Oxide Fuel Cells: Fundamentals, Design, and Applications*, S.C. Singhal and K. Kendell, Editors. 2003, Elsevier Ltd.: Bodmin.
41. Primdahl, S., *Gas diffusion impedance in characterization of solid oxide fuel cell anodes.* Journal Of The Electrochemical Society, 1999. 146(8): p. 2827-2833.
42. DeCaluwe, S.C., *Importance of anode microstructure in modeling solid oxide fuel cells.* Journal Of The Electrochemical Society, 2008. 155(6): p. B538-B546.